Neutrophils exhibit distinct migration phenotypes that are modulated by transendothelial migration

Amy B. Schwartz[1], Adithan Kandasamy[2,3,4], Juan C. del Álamo[2,3,4,5]*, Yi-Ting Yeh[2,3,4]*

[1] Department of Mechanical and Aerospace Engineering, University of California San Diego, La Jolla, CA

[2] Department of Mechanical Engineering, University of Washington, Seattle, WA

[3] Center for Cardiovascular Biology, University of Washington, Seattle, WA

[4] Institute of Stem Cell and Regenerative Medicine Cardiovascular Biology, University of Washington, Seattle, WA

* corresponding authors:

Juan C. del Álamo: juancar@uw.edu

Yi-Ting Yeh: yiyeh@uw.edu

Abstract

The extravasation of polymorphonuclear neutrophils (PMNs) is a critical component of the innate immune response that involves transendothelial migration (TEM) and interstitial migration. TEM-mediated interactions between PMNs and vascular endothelial cells (VECs) trigger a cascade of biochemical and mechanobiological signals whose effects on interstitial migration are currently unclear. To address this question, we cultured human VECs on a fibronectin-treated transwell insert to model the endothelium and basement membrane, loaded PMN-like differentiated HL60 (dHL-60) cells in the upper chamber of the insert, and collected the PMNs that crossed the membrane-supported monolayer from the lower chamber. The 3D chemotactic migration of the TEM-conditioned PMNs through collagen matrices was then quantified. Data collected from over 50,000 trajectories showed two distinct migratory phenotypes, i.e., a high-persistence phenotype and a low-persistence phenotype. These phenotypes were conserved across treatment conditions, and their existence was confirmed in human primary PMNs. The high-persistence phenotype was characterized by more straight trajectories and faster migration speeds, whereas the low-persistence one exhibited more frequent sharp turns and loitering periods. A key finding of our study is that TEM induced a phenotypic shift in PMNs from high-persistence migration to low-persistence migration. Changes in the relative proportion of high-persistence and low-persistence populations correlated with GRK2 expression levels. Inhibiting GRK2 hindered the TEM-induced shift in migratory phenotype and impaired the phagocytic function of PMNs. Overall, our study suggests that TEM-mediated GRK2 signaling primes PMNs for a migration phenotype better suited for spatial exploration and inflammation resolution. These observations provide novel insight into the biophysical impacts of TEM that priming PMNs is essential to conduct sentinel functions.

Introduction

Polymorphonuclear neutrophil (PMN) migration to sites of injury or infection is a primary component of innate immunity and inflammatory responses (1, 2). Upon encountering the signals associated with injured or inflamed tissue, circulating PMNs escape blood vessels by adhering to and probing inflamed vascular endothelial cells (VECs), breaching endothelial cell-cell junctions, and transmigrating across the endothelium before infiltrating the surrounding tissue (3). This process, known as trans-endothelial migration (TEM), is a rate-limiting step in the immune response (1). Transmigrated PMNs efficiently navigate 3D tissue-like environments to reach their targets (4-6). The interactions between PMNs and VECs during TEM modulate several PMN characteristics, including their life span and effector function (7, 8). However, while the initial recruitment of PMNs has been extensively characterized (1, 3), the effect of TEM on their subsequent interstitial migration behavior, and the correspondence between resulting migration phenotype and effector function, remain largely unknown.

There are two mechanisms whereby PMNs can traverse the VEC monolayer and exit the circulation: paracellular TEM through the junctions between VECs and transcellular TEM through thin portions of the endothelial cell body (1). The paracellular route is the most common, comprising over 90% of transmigration events (9). Paracellular TEM is facilitated by interactions with many endothelial-expressed surface adhesion molecules, including vascular endothelial cadherin (VE-cadherin), platelet/endothelial-cell adhesion molecule 1 (PECAM1), various junctional adhesion molecules, and other selective adhesion molecules such as ICAM-1 (3, 10). TEM is also known to induce PMN surface expression of the β1-integrin family and β2-integrins, such as lymphocyte function-associated antigen 1 (LFA1) and macrophage-1 antigen (CD11b) (1). Mechanically, PMNs extend invadosome-like protrusions to dynamically probe the underlying endothelium and potentially identify the path of least resistance (11). Subsequently, they actively contract over the VECs, leading to junctional gap openings, and force themselves through the gaps (12). VECs also play an active role in PMN trafficking, forming actin-rich ICAM-1 projections known as “docking structures” that help to anchor and embrace the leukocyte and have been speculated to facilitate extravasation by generating contractile stresses to pull PMNs into and across the VEC monolayer (13, 14). Because PMN sizes can be more than 20 times greater than the size of endothelial cell-cell junctions (~10 μm vs. ~0.5 μm), transmigrating through VEC junctions can cause unusually high PMN deformations (15). Mechanical constriction at VEC junctions has been suggested to influence PMN transmigration and subsequent interstitial migration towards infection sites (7).

73 *In vivo*, the extravascular space is a complex, highly dynamic, and densely packed environment
74 composed of collagen fibers, glycoproteins, and other ECM fibers. As such, transmigrated PMNs
75 need to negotiate crowded spaces with varying pore sizes to reach the site of inflammation (6,
76 16, 17). In 3D environments, PMNs utilize integrin-independent migration, relying on actin
77 cytoskeletal-network expansion to generate protrusive forces along the leading edge, coupled
78 with myosin-II dependent contractility to bring up the rear (18, 19). To perform efficient pathfinding
79 in 3D, PMNs alternate frequent turns with directional persistence to steer themselves toward the
80 chemotactic gradient (4). This alternance involves intermittent, integrin-mediated periods of
81 traction force exertion (20). Cell migration in 2D is typically modeled as a persistent random walk
82 (PRW), which depends on two critical motility parameters: migration speed and persistence (21-
83 24). However, the complexity of cell-ECM interaction in restrictive 3D environments introduces
84 modeling difficulties (25). Also, single cells moving in 3D can rapidly transition between slow and
85 fast migration states, making it necessary to contemplate time-varying parameters in random walk
86 models (26). In addition to these dilemmas, PMNs can exhibit distinct phenotypic diversity and
87 plasticity in crucial functions, including their migratory behavior (27-30). For example, successful
88 clearance of bacterial infection depends on efficient PMN migration into the infected tissues,
89 including a stop signal that helps resolve inflammation (31). However, phenotypic diversity in
90 migration is rarely considered in experimental analysis and remains poorly understood.

91 The early response of PMNs to a chemoattractant gradient increases migration speed and
92 persistence towards the chemoattractant focus. In contrast, these migratory parameters are
93 suppressed in late response phases as high chemoattractant concentrations desensitize surface
94 G-protein coupled receptors (GPCRs) on the cell surface (32-34). The multifunctional GPCR
95 kinase GRK2 was recently linked to PMN swarm resolution via receptor desensitization, with
96 GRK2-deficient PMNs also demonstrating impaired bacterial clearance by inefficiently picking up
97 and ingesting microbes from bacteria clustering (31). In addition to its classical role in modulating
98 GPCR signaling through receptor internalization and recycling, GRK2 is known to function as a
99 signaling hub via phosphorylation and scaffolding interactions with myriad non-GPCR partners
100 (35). Of note, GRK2 has been shown to negatively regulate immune response via direct
101 association with the MAPK kinase MEK (36) and to phosphorylate the membrane-cytoskeletal
102 linkers ezrin (37) and radixin (38), suggesting a direct link between GRK2 expression and actin
103 cytoskeleton reorganization. Based on these results, GRK2 presents an intriguing link between
104 PMN migration phenotype and effector functionality.

This work's central hypothesis is that the biomechanical PMN-VEC interactions associated with TEM modulate PMN functions to promote the efficient identification and elimination of pathogens. To address this hypothesis, we employed an experimental assay with two subsequent stages. The first stage is a transwell-based TEM model, and the second stage is a physiologically relevant 3D collagen directional migration assay. Using this in vitro model, we characterized the migratory and functional changes induced by TEM of nearly 50,000 individual dHL-60 and primary PMN cells. We used sequential and variational Bayesian inference algorithms to identify two naturally occurring, phenotypically distinct migratory subpopulations conserved across treatment conditions. The first is a high-persistent phenotype characterized by a fast, directed migration toward chemoattractant sources. The second is a low-persistent phenotype characterized by a slower, more random migration. The relative prevalence of these phenotypes is modulated by TEM-mediated changes in PMN expression of GRK2. These findings show a critical role for TEM in determining the subsequent PMN interstitial migration phenotypes, demonstrating that VECs can modulate PMN migration to promote immune function.

Results

TEM modulates transcription and protein expression of chemokine receptors and increases phagocytic function

To model the impact of PMN trans endothelial migration (TEM) on subsequent interstitial 3D migration, we developed a two-stage *in vitro* assay that combines a commercial transwell migration assay and a previously described 3D-migration chamber (4) (Figures 1A and 2A). We performed real-time quantitative PCR (RT-qPCR; Figure 1B) and flow cytometry (FCS; Supplementary Figure 1A) to compare intracellular gene expression and cell surface protein expression, respectively, of selected chemokine receptors, surface integrins, and glycoproteins before and after cells crossing the VEC-coated transwell insert (**ETW**-conditioning). These data collectively demonstrate upregulation of CD11b, ICAM-1, and FPR1 (for RT-qPCR, ICAM-1: $p = 0.0024$; FPR1: $p = 0.0172$) in conjunction with downregulation in CXCR2 (for RT-qPCR, $p = 0.003$) and decreased cell surface expression of CXCR1 (for RT-qPCR, $p > 0.9999$). These changes are all qualitatively consistent with PMNs that have undergone TEM *in vivo* (39), suggesting that TW crossing altered the expression profile of dHL-60 cells in a similar manner.

PMNs utilize their G-protein-coupled chemokine receptors (GPCRs) to detect chemoattractants (40). Two receptors, CXCR1 and CXCR2, have been reported to coordinate PMN directional motility through differential surface expression levels, promoting PMN clustering at the infection site and facilitating the posterior self-resolution of PMN clusters (34). The down-regulation of CXCR1 and CXCR2 gene and surface expressions with ETW crossing prompted us to investigate how TEM impacted PMN directional migration and phagocytic function. Thus, we conducted additional experiments using dHL-60 cells co-cultured with VECs without transmigration (co-culture condition, **CC**) and loaded into unmodified transwell inserts (transwell only condition, **TW**) to decouple the contribution of VECs and the cellular deformation experienced by PMNs squeezing through narrow transwell membrane pores (Figure 1C). We performed flow cytometry to detect surface expressions of CXCR1 and CXCR2 in these four conditions, finding that the surface expressions of both CXCR1 and CXCR2 decrease significantly in TW- and ETW-conditioned cells (Figures 1D-E). In contrast, the expression of CXCR2 did not decrease significantly after CC conditioning. Taken together, these results suggest that the surface expressions of PMN chemokine receptors are mechanosensitive and that biochemical interactions with VECs may regulate surface trafficking of CXCR1 and CXCR2 through different mechanisms.

151 It is important to note that the CXCR2 fluorescence intensity profiles exhibited a marked shift to
152 low values for TW- and ETW-conditioned cells (Supplementary Figure 1B). The large magnitude
153 of this shift allowed us to discard the possibility that the changes in CXCR2 with respect to controls
154 were the result of a selection process, i.e., that cells with low CXCR2 expression values were
155 more successful at crossing the transwell membrane pores, because cells with such low levels of
156 CXCR2 expression did not originally exist in the control and CC-treated groups. Therefore, we
157 concluded that these changes were a phenotypic change induced by TW- and ETW-conditioning.

158 Next, we used pHrodo GFP-conjugate zymosan to assess changes in PMN phagocytosis ability
159 following these treatments. Zymosan particles do not fluoresce outside of the cells or inside of the
160 cell cytosol due to these environments' neutral pH. However, when phagocytes internalize the
161 particles into the acidic environments of endosomes and lysosomes, the GFP dye fluoresces
162 brightly, reporting bacterial ingestion into PMN phagosomes. Flow cytometry results showed
163 almost 90% of TW- and ETW-conditioned cells were GFP-positive for bacterial ingestion (Figure
164 1F). In comparison, only 40% of CC-conditioned cells and 20% control cells were GFP-positive
165 (Figure 1G). These data demonstrate that mechanical stimuli in the TEM process can activate the
166 PMN phagocytic machinery.

167 **The persistence of PMN migration through 3D collagen matrices is heterogeneous**

168 To study the impact of TEM on the subsequent PMN migration through 3D matrices, we tracked
169 and analyzed the motion of approximately 50,000 control, CC, TW-, and ETW-conditioned cells
170 in 1 mg/mL collagen under an fMLP chemoattractant gradient as previously described (4) (Figures
171 2A-B). Figure 2C shows representative trajectories for chemotaxing dHL-60 cells in each
172 condition superimposed onto probability density maps of their endpoint positions. A red dashed
173 circle representing non-chemotactic random migration is included for reference. Control cells
174 migrated directionally up the fMLP gradient as expected (4), but cells from all other conditions
175 described omnidirectional trajectories. In particular, the cells from the TW, ETW, and CC appeared
176 to have an increased propensity to migrate against the gradient and to incorporate large-angle
177 turns in their migration (see arrows in Figure 2C), similar to those reported in late phases of the
178 immune response when PMNs are desensitized to the chemoattractant (31). As a result of these
179 behaviors, TW, ETW, and CC cells had significantly lower mean chemotactic indices than controls
180 (Figure 2D) even if their mean speed was higher (Figure 2E). These results are consistent with
181 the changes in CD11b, CXCR1, and CXCR2 reported in the previous section, further suggesting
182 that TEM predisposes PMNs to adopt a more active, exploratory interstitial migration phenotype.

To quantify in more detail how TW, ETW, and CC conditions impacted the cell trajectories, we computed the mean squared displacements (r^2 or MSD, Figure 2F) and autocorrelation function of the vector tangent ($\vec{t}$) to the cell trajectory (C_{tt}, Figure 2G) versus distance traveled (Δs). Because the MSD plot is obtained by integrating the C_{tt} plot twice with respect to Δs, it experiences quadratic growth ($r^2 \sim \Delta s^2$) near the origin. As C_{tt} falls when Δs increases, the MSD plot tapers to behave linearly ($r^2 \sim \Delta s$) for very long distances. This attenuation in slope reflects the loss of overall migratory persistence when migrating in 3D across large distances, as cells encounter obstacles in the microenvironment and need to circumvent them. Despite their slight differences, the MSD of TW, ETW, CC, and control cells were similar (Figure 2F), suggesting all cell trajectories had similar persistence at the population level, even if control cells were persistent and also aligned with the chemoattractant gradient while TW, ETW, CC cells were persistent and omnidirectional.

Inspection of C_{tt} revealed more complex behavior with two distinct exponential decays, evidenced as two straight segments in each curve of the linear-logarithmic plot in Figure 2G. In all conditions, there was steep initial decay in C_{tt} over displacements of 0 μm to 10 μm followed by a shallower decay over much longer distances. The existence of two regimes in C_{tt} suggests that the studied cell populations may exhibit heterogeneous migratory behavior in terms of directional persistence, with the steeper segments corresponding to a less motile phenotype than the shallow segments. This possibility is evaluated in detail in the next section. We estimated the persistence length (L_p) of cell trajectories in each condition by performing an exponential fit to the shallower decay segment (see Materials and Methods). The results of this analysis (Figure 2H) indicate that TW- and ETW-conditioned cells experienced a modest albeit significant decrease in L_p, consistent with a more exploratory migratory behavior.

PMNs exhibit distinct migratory phenotypes whose prevalence is modulated by TEM

Motivated by the results in the previous section, we investigated the existence of distinct migratory phenotypes in PMN cell populations and how TEM affects their relative frequencies. We fitted each cell's trajectory to a random walk model with time-dependent parameters q_t and a_t (see Materials and Methods) (26). In this model, q_t represents the persistence of the motion and a_t its activity, or instantaneous speed of random motion. We then plotted probability density contours of (q_t, a_t) for each of the four conditions studied: TW, ETW, CC, and control (Figures 3A-D). The probability contours obtained for control cells were clearly bimodal (Figure 3A), revealing two distinct migratory phenotypes. The most abundant one was formed by cells of high persistence

215 and activity, whereas the other consisted of significantly less persistent and slightly less active
216 cells. We named them high-persistence and low-persistence phenotypes and observed their
217 presence in the other conditions. In TW-conditioned cells, the high-persistence phenotype was
218 very dominant, and the low-persistence one was virtually nonexistent (Figure 3B). Conversely,
219 the high-persistence phenotype was less abundant, and the low-persistence phenotype was more
220 prevalent in ETW-conditioned and CC-conditioned cells than in controls (Figure 3C and 3D,
221 respectively).

222 To confirm the existence of distinct motility phenotypes, we ran a quasi-unsupervised clustering
223 algorithm rooted in variational Bayesian inference for a Gaussian Mixture Model (VB-GMM, see
224 Materials and Methods). The VB-GMM algorithm was tasked with identifying four clusters in
225 (q_t, a_t) space from the pooled distribution of all the studied dHL-60 cells (Supplementary Figure
226 2A). Visual inspection of the cell trajectories belonging to the least abundant cluster (extremely
227 high activity levels, <10% of the total cell population) revealed that these trajectories had obvious
228 cell tracking errors. As such, this subgroup was labeled "Discard", and its tracks were excluded
229 from further analysis. The remaining two clusters identified by the VB-GMM algorithm were neatly
230 aligned with the two modal peaks in the probability contours of Figures 3A-D and were, therefore,
231 similarly denoted as high- and low-persistence clusters (Supplementary Figure 2B).

232 Figure 3E shows examples of trajectories belonging to each cluster for each of the conditions
233 studied, confirming that high-persistence trajectories were long and relatively straight, whereas
234 low-persistence trajectories described numerous turns and covered less distance. Figure 3F
235 quantifies the relative prevalence of each motility cluster across all studied conditions, indicating
236 that control cells had nearly an even split between low- and high-persistence trajectories (48.9%
237 high, 50.2% low) and that this split changed for TW-conditioned, ETW-conditioned, and CC-
238 conditioned cells. Consistent with the probability maps described above, the high-persistence
239 trajectories became more frequent in TW-conditioned cells (60.7% high, 36.4% low). Likewise,
240 the low-persistence trajectories became more frequent in ETW-conditioned cells (30.6% high,
241 65.5% low) and CC-conditioned cells (29.1% high, 61.0% low).

242 These experiments demonstrate that dHL-60 cells exhibit a heterogeneous migratory behavior
243 characterized by two distinct phenotypes: a direct migration phenotype and a more wandering
244 phenotype. Our data also suggests that TEM predisposes dHL-60 cells to switch from the direct
245 phenotype to the wandering phenotype. Taken together, our results support that signaling induced
246 by interactions with the VECs plays a dominant role in promoting the interstitial migratory

247 phenotype of dHL-60 cells after TEM. In our experiments, VEC-dHL60 contact eclipsed the
248 phenotypic change induced by mechanical deformation alone (ETW condition).

249 **Primary human PMNs display high- and low-persistence migratory phenotypes as**
250 **observed in dHL-60 cells**

251 DMSO differentiated HL-60 cells are often employed as a PMN model as their migration and
252 function are qualitatively similar to primary PMNs (41). To elucidate if the existence of two
253 migratory phenotypes represents primary PMN behavior, we repeated the 3D interstitial migration
254 experiments and subsequent analyses with primary PMNs derived from whole human blood
255 (Materials and Methods). The probability density contours of (q_t, a_t) for primary PMNs, shown in
256 Figure 4A, agreed qualitatively with those obtained from dHL-60 cells, overlaid for reference in
257 the figure. More specifically, PMNs exhibited a low-persistence mode that co-localized with the
258 low-persistence mode of dHL-60 cells in the (q_t, a_t) space. Besides, the primary PMN probability
259 density map displayed a long horizontal plateau with similar persistence values and equal or
260 higher activity values than those of the dHL-60 high-persistence mode. We identified this plateau
261 as the primary PMN high-persistence mode.

262 When applied to the pooled dataset of tracked primary PMN trajectories, the VB-GMM algorithm
263 independently identified distinct high-persistence and low-persistence clusters (Figure 4B).
264 Moreover, these clusters occupied similar regions of the (q_t, a_t) space as dHL-60 cells, even if
265 primary PMNs were skewed slightly toward higher activity values overall. Example trajectories
266 obtained from the low- and high-persistence clusters had similar appearances in dHL-60 cells and
267 primary PMNs (Figure 4C-D). On the other hand, the relative frequency of high-persistence
268 migration was lower in primary PMNs s (15.4%) than in dHL-60 cells (48.9%), as shown in Figure
269 4E.

270 Summary migration statistics were computed separately for the high- and low-persistence clusters
271 of primary PMNs to permit a quantitative fine-grained comparison with dHL-60 cells. For
272 quantifying effective migration statistics, we excluded the non-motile cells (Supplementary Figure
273 2A). The mean cell speeds of both cell types in the high-persistence cluster were significantly
274 different, with primary PMNs in the control condition moving approximately twice faster than dHL-
275 60 cells in all conditions (Figure 5A). In the low-persistence cluster, the cell speeds of control
276 condition of dHL-60 cells and primary PMNs still showed statistically significant differences, but
277 the differences in magnitude were modest (Figure 5B). Likewise, TW, ETW, and CC conditioning
278 increased the speed of dHL-60 cells in both clusters, but these differences were considerably
279 smaller than the differences between clusters. When analyzing the chemotactic efficiency of cells

280 belonging to each subgroup (Figure 5C-D), we found that TW, ETW, and CC conditioning caused
281 a >50% reduction in CI in both the high- and low-persistent clusters, bringing the net CI to near
282 zero values (<0.1) in the low-persistent cluster. Of note, ETW and CC conditioning brought the
283 chemotactic efficiency of dHL-60 cells to values similar to primary PMNs. These data suggest that
284 VEC interactions are crucial for dHL-60 cells to better recapitulate primary cell characteristics.

285 **TEM-induced low-persistence migration involves zigzagging**

286 Previous studies (4, 25) have uncovered hidden features of 3D cell migration using the probability
287 distribution of turning angles conditional to the distance traveled along each cell's trajectory,
288 $p(\Delta\theta|\Delta s)$. Thus, we computed this distribution for the high- and low-persistence trajectories of
289 primary PMNs and dHL-60 cells in all conditions studied. The $p(\Delta\theta|\Delta s)$ maps from the control
290 dHL-60 cells belonging to the high-persistent cluster (Figure 5E) displayed a narrow peak around
291 $\Delta\theta = 0$ for short distances Δs, which broadened as Δs increased. This behavior has been attributed
292 to cells incorporating turns in their trajectories to circumvent environmental obstacles, leading to
293 a progressive loss of directional memory with increasing spatial separation (4). Highly motile dHL-
294 60 cells in the TW, ETW, and CC conditions exhibited similar $p(\Delta\theta|\Delta s)$ distributions (Figure 5E).

295 Cells assigned to the low-persistence cluster (Figure 5F) exhibited markedly different distributions
296 of turning angles. The low-Δs peak around $\Delta\theta = 0$ was broader than in the high-persistence
297 cluster, suggesting a propensity to describe slightly less straight segments at short distances
298 compared to cells in the high-persistence cluster. Moreover, a second prominent peak appeared
299 around $\Delta\theta = p$ for Δs > 10 mm, indicating an increase in the frequency of ≈180-degree turns.
300 Inspection of individual migration tracks suggest that this occurs because cells began
301 implementing abrupt changes of direction alternating with relatively straight segments, i.e., a
302 zigzagging behavior (42) (Supplement Figure 3). The turning angle distributions for cells in the
303 TW, ETW, and CC conditions had similar bimodal features (Figure 5F).

304 The similarities in the $p(\Delta\theta|\Delta s)$ of control, TW-, ETW-, and CC-conditioned cells within each
305 cluster confirm that these motility clusters represent distinct and well-defined migration
306 phenotypes that are conserved across dHL-60 treatment conditions. Importantly, the bimodal
307 turning angle distribution seen in dHL-60 cells was also observed in primary PMNs and was more
308 prominent in the low-persistence cluster (Figure 5E-F). Zigzagging migration patterns have been
309 observed in PMNs *in vivo* and have been proposed to help find sparsely distributed targets (42).
310 Our data suggests these phenotypes, particularly the low-persistence phenotype, are preserved
311 across primary PMNs and dHL-60 cells with high level of detail in terms of trajectory morphology.

312 **TEM-mediated leukocyte expression of GRK2 controls PMN's ability of directional**
313 **migration and phagocytosis**

314 The existence of distinct migratory phenotypes in PMN migration through 3D matrices, and the
315 modulation of their relative prevalence on TEM-associated external stimuli motivated our
316 investigation of molecular signals involved in this modulation. Recent *in vitro* experiments of
317 murine PMN migration demonstrated that GRK2-deficient PMNs exhibit faster, more persistent
318 migration in response to but irrespective of the direction of externally imposed gradients of the
319 intermediate chemoattractant LTB4 (31). Due to the stark shift in migration phenotype seen in
320 knockdown cells, GRK2 immediately became a candidate molecule to explain the differences in
321 track tortuosity between the high- and low-persistence clusters observed in our experiments.

322 Figure 6A shows RT-qPCR results for GRK2 expression in the four conditions studied: control,
323 TW, ETW, and CC. Even if these data demonstrate potential for kinase expression rather than
324 actual kinase activity, the statistically significant increases seen in TW- and ETW-conditioned
325 dHL-60 cells are consistent with the observed population-level losses in chemotactic index.
326 Notably, the expression levels in ETW- and CC-conditioned cells were indistinguishable ($p >$
327 0.9999), suggesting endothelial interaction is sufficient to induce moderate PMN GRK2 increases.
328 Compared to the stark GRK increase in the TW conditioned, such moderate GRK expressions in
329 ETW-conditioned cells suggest that endothelial interactions may blunt the effect of TEM-mediated
330 mechanical deformation on PMN chemotactic migration.

331 We inhibited GRK2 expression in control and ETW-conditioned cells with the potent, selective
332 GRK2 inhibitor CMPD101 and assessed the impact on 3D leukocyte migration before and after
333 ETW-conditioning. CMPD treatment rendered control dHL-60 cells effectively non-motile
334 (Supplementary Figure 4), probably because lower constitutive expression of GRK2 made them
335 unable to perform GPCR trafficking after inhibition. However, and interestingly, the treatment had
336 its anticipated effect on the migration ETW-conditioned cells. Cell trajectories became highly
337 directional and covered more space (Figure 6B), and their mean speed (Figure 6C) and
338 chemotactic index (Figure 6D) increased significantly. Their MSD and C_{tt} (Figure 6E-G) were
339 suggestive of increased directional persistence, which was confirmed by computing the
340 persistence length L_p and comparing it to that obtained in CMPD-untreated TW- and ETW-
341 conditioned cells (Figure 6G).

342 In addition to analyzing the migratory behavior of dHL-60 cells after pharmacological GRK2
343 inhibition, we studied how this inhibition affected the cells' phagocytic activity, since this function
344 is crucial to the innate immune response. In particular, we evaluated *in vitro* phagocytosis of

ETW-conditioned dHL-60 cells with and without CMPD treatment by exposing these cells to zymosan bioparticles (see Materials and Methods). The results from this experiment (Figure 6H) showed that the inhibition of GRK2 activity in the ETW-conditioned cells significantly attenuated TEM-mediated improved zymosan bioparticle ingestion.

GRK2 controls the TEM-mediated shift from high-persistence to low-persistence interstitial migration

To investigate how GRK2 modulates TEM-mediated changes in migratory phenotype, we tracked and analyzed the trajectories of CMPD-treated, ETW-conditioned dHL-60 cells migrating in our 3D collagen chemotactic device. The resulting probability maps of (q_t, a_t) were plotted in Figure 7A, together with reference contours from CMPD-untreated, TW-conditioned (grey circles) and ETW-conditioned (red triangle) cells. These data show that CMPD treatment shifted the migratory phenotypic distribution of ETW-conditioned cells towards the distribution observed for CMPD-untreated, TW-conditioned cells. The shift was confirmed by the relative prevalences of low- and high-persistence clusters obtained with the VB-GMM classifier (Figure 7B). Specifically, GRK2 inhibition eliminated nearly 75% of the low-persistence population in TW-conditioned cells (TW: 65.50%; TW CMPD: 17.45%). When compared with human primary PMNs, the CMPD-treated ETW-conditioned dHL-60 cells had opposite proportions of high- and low-persistence clusters (Figure 7B).

Trajectories representative of the high- and low-persistence clusters in CMPD-treated ETW-conditioned cells (Figure 7C) were not strikingly different from those of untreated cells, albeit the low-persistence trajectories in the CMPD-treated cells seemed to zigzag less often. CMPD treatment caused a statistically significant albeit modest mean speed increase in both clusters (Figure 7D). The effect of treatment on the chemotactic index (Figure 7E) was more interesting. While this parameter was not affected by treatment in the high-persistence cluster, it experienced a dramatic increase in the low-persistence cluster. To interpret this result, it is important to keep in mind that the low-persistence cluster in ETW-sorted CMPD-treated cells had low prevalence, so this cluster's high mean CI might be influenced by having sampled cells from the tail of the more abundant high-persistence cluster. This would be consistent with the high- and low-persistence clusters having similar values of CI after CMPD treatment (Figure 7E). In any case, the main result that holds independent of these methodological details is that cells with low chemotactic efficiency were hardly observed after CMPD treatment.

Altogether, these data show that TEM enhances PMN host-defense function through upregulation of GRK2. The data supports the hypothesis that GRK2 expression is responsible for the tortuous,

a chemotactic migration phenotype observed in low persistent cells. Furthermore, CMPD treatment of ETW-conditioned cells recapitulated the migratory mode distribution of TW cells, supporting a role for VEC interaction in modulating GRK2 expression. When considered together, these results implicate GRK2 expression as the controlling modulator of the low-persistence phenotype prevalence, circumstantially supporting the conclusion that intercellular interactions during junctional trafficking are responsible for modulating PMN expression of GRK2.

Discussion

PMNs are specialized immune cells circulating in the bloodstream that extravasate to migrate toward pathogens localized in the surrounding tissues. However, PMNs exhibiting fast, persistent migration often fail to contain bacteria growth *in vivo* (31). Instead, the ability to slow down and stop responding to chemoattractants seems to be essential for bacterial containment. Therefore, extravasated PMNs must exhibit plasticity in their migratory and phagocytic activity but the mechanisms that regulate this plasticity are still unclear. This study focused on how TEM, a crucial step of PMN extravasation, affects the migratory phenotype of PMNs and associated effector functions like phagocytosis.

Bayesian inference (26) of random walk in single cell trajectories yields time-varying values for two parameters representing each cell's migratory persistence and random activity. Machine learning analysis of these two parameters for nearly 50,000 trajectories of PMNs migrating through 3D collagen matrices identified two distinct migratory phenotypes. One was characterized by fast, directed, chemotactically efficient *high-persistence* migration. The other was characterized by a slower, tortuous, *low-persistence* migration. Summary statistics like cell speed or chemotactic index have been used for decades to quantify the efficiency of PMN migration toward infection sites. Given the inherent variability of biological data, it is customary to average these statistics over multiple cells recorded under similar experimental conditions, assuming they all exhibit similar behavior. The heterogeneous migratory behavior of PMNs challenges this assumption and calls for caution when interpreting summary statistics computed over entire cell populations.

The low- and high-persistence migration phenotypes were present in dHL-60 cells across all different conditions studied and conserved in human blood PMNs. In line with this robustness, fast and slow subpopulations of neutrophils have been observed in the swarming locus of a murine ischemic-reperfusion injury model (43). More recently, we have reported heterogeneous migratory phenotypes in 3D-migrating T cells *in vitro* (44). Similarly, NK cells have been seen to intermittently exhibit in high- and low- persistence migratory modes depending on traction force exertion (20). The heterogeneity of migratory states is emerging as a preserved characteristic across different immune cells, further motivating the need to delineate how it is regulated since transitions between states could be a mechanism that endows PMNs with plasticity.

Our data suggest that TEM-associated stimuli promote a shift from the high- to the low-persistence migratory phenotype. TEM involves large PMN deformations and multiple molecular interactions with VECs that can cause mechanobiological responses (3, 8). For instance, dHL-60

417 cells traversing narrow constrictions experience chromatin reorganization (45), and prolonged
418 cyclic deformations have been shown to depolarize PMNs (46). Experiments on human PMNs
419 migrating up an fMLP gradient inside tapered microfluidic channels suggest that increasing
420 mechanical confinement can trigger reverse chemotaxis (47). Reverse migratory behavior
421 induced by physical constraints has been suggested to facilitate inflammation resolution (48).

422 In our experiments, crossing an empty membrane without VECs, an assay that only causes PMN
423 deformation, predisposed dHL-60 cells to perform high-persistence migration contrary to our
424 observations in VEC-lined membranes. This result suggests that heterotypic cell interactions
425 during TEM could be significant modulators of PMN phenotype, overriding mechanical stimuli.
426 Our experiments used 3-μm transwell membrane pores, as previously described (8), to allow
427 enough cells to transmigrate and be collected for the 3D migration assay. Such pore size
428 significantly exceeds the estimated endothelial junctional gap size (49), so our *in vitro* model could
429 underrepresent PMN deformation. However, the transwell membrane material, polyethylene
430 terephthalate (PET), is orders of magnitude stiffer than the VEC monolayer and the underlying
431 basement membrane, which should compensate for the larger pore size.

432 We used a robust unsupervised clustering method to identify distinct migratory phenotypes (50,
433 51) based on parameterizing cell trajectories using a persistent random walk (PRW) model. The
434 standard PRW model has been widely utilized for analyzing and simulating the migration of many
435 cell types over flat surfaces (21-24) and has the convenience of relying on few parameters.
436 However, applying this model to 3D cell migration has been more challenging (25). Studies relying
437 on 4D live imaging produce hundreds of morpho-kinetic parameters per cell to help understand
438 individual PMNs' dynamic behavior under inflammation (43). However, phototoxicity, limited time
439 resolution, and overall low throughput limit this approach to low numbers of cells that impede
440 advanced statistical analyses. We utilized large-scale, label-free cell tracking to obtain multiple
441 high-resolution trajectories per experimental video (4), incorporating a heterogeneous PRW
442 model with time-dependent parameters that better captures the multi-scale patterns of 3D cell
443 migration than the standard PRW model (26). An example of such patterns is the zigzagging
444 described by cells belonging to the low-persistence cluster, which combines fast, highly-
445 persistence segments with slower, quasi-random segments.

446 Although dHL-60 cells are a valid model system for many PMN studies (52), their imperfect
447 differentiation efficiency and replication of PMN functions posit some limitations (41, 53).
448 Therefore, we assayed PMNs obtained from human blood in our 3D migration device to validate
449 our key findings in dHL-60 cells, e.g., the existence of two migratory phenotypes or the defining

450 characteristics of each phenotype. Summary statistics like mean cell speed agreed with
451 previously published results for dHL-60 cells and human PMNs (52). A more detailed comparison
452 of cell trajectories based on the probability distribution of turning angles indicated a high level of
453 similarity between human PMNs and the low-persistence cluster of dHL-60 cells. In particular,
454 both cell types exhibited a clear secondary probability peak for large-angle turns, i.e., the hallmark
455 of zigzagging. In this low-persistence cluster, dHL-60 cells from the ETW and CC conditions were
456 most similar to human blood PMNs in terms of mean speed and CI, implying that TEM-mediated
457 interactions with VECs could predispose dHL-60 cells to adopt a more physiologically
458 representative phenotype. Also, PMNs from blood draws may have experienced diverse VEC
459 interactions before collection, such as traversing the bone marrow endothelium or transmigrating
460 from tissues back into the bloodstream (54, 55). These interactions could explain the similarity
461 between human PMNs and ETW- and CC-conditioned dHL-60 cells.

462 GRK2 is an integrative signaling hub for modulating various aspects of cell migration processes
463 (35). Upon chemokine stimuli, GRK2 constitutes serine/threonine protein kinases that specifically
464 phosphorylate G protein-coupled receptors (GPCRs) to desensitize receptors (36). PMN
465 swarming is a collective, self-amplifying response in which multiple PMNs form a perimeter
466 around damaged tissue to prevent the spread of infection. GRK-2 deficient PMNs have exhibited
467 reduced migration arrest and hence, ineffective swarm resolution (31, 56). Our experiments
468 showed that GRK2 expression was enhanced in ETW-conditioned dHL-60 cells and that these
469 cells had increased phagocytosis concurrent with a shift to the low-persistence phenotype.
470 Moreover, GRK2 inhibition after ETW-conditioning blunted phagocytic activity and steered cells
471 toward the high-persistence migratory phenotype. Therefore, our data suggest that TEM
472 promotes a PMN phenotype with less persistent migration and increased phagocytic activity via
473 upregulating GRK2 signaling.

474 It is possible that TEM stimulates a low-persistence migratory phenotype in PMN by degrading
475 CXCR2 via GRK2 activation, consistent with evidence that GRK2 facilitates CXCR2
476 internalization and degradation (57). In agreement with this idea, we found that TW- and ETW-
477 conditioned dHL-60 cells exhibited significant downregulation of CXCR2 surface expression.
478 Moreover, our finding that CC conditioning did not change the expression level of CXCR2
479 suggests that the TEM-mediated modulation of this receptor could depend on mechanical stimuli.
480 Low CXCR2 expression could be a natural modulator of PMN subpopulations. Indeed, a low-
481 CXCR2-expression PMN cluster has been reported independently in different single-cell
482 sequencing analyses (58, 59). Analysis of cell states showed that this cell cluster exhibits stronger

483 anti-microbial activity than clusters with higher CXCR2 expression. Nevertheless, we cannot rule
484 out that the molecular and surface changes of CXCR2 observed in our experiments result from
485 other processes, including nuclear deformation-induced transcriptional changes or non-GRK2
486 activation-mediated CXCR2 expression. Experimental and analysis platforms such as the one
487 presented here are poised to provide detailed, large-scale quantification of migratory behavior to
488 help answer these questions.

489 Our study revealed that TEM-associated stimuli significantly affect the phenotype of PMNs. We
490 showed increased phagocytic activity and concomitant loss of migratory persistence in PMNs
491 after TEM, modulated by heterotypic interactions with VECs and mechanical deformation
492 associated with junctional trafficking. Heterotypic interaction of dHL-60 with VECs recapitulates
493 key migration features of primary PMNs in the low-persistence subpopulation, suggesting a more
494 physiological relevant cell-line protocol of PMNs. Mechanical deformation during TEM is
495 necessary for PMN functions in addition to heterotypic cell-cell interaction. GRK2 upregulation
496 due to both effects from the TEM process is crucial for modulating PMN phenotype changes
497 related to efficient pathogen identification and clearance. Immunosuppressants for treating
498 chronic inflammation have numerous adverse side effects, including an increased risk of
499 infections. Our findings on how the TEM process modulates PMN migration and functional
500 plasticity may provide a rationale to identify specificity in targeting only one population of PMNs,
501 thus offering opportunities for treating inflammation without compromising PMN's anti-infection
502 defense mechanisms.

503 **Materials and Methods**

504 **Cell culture and differentiation**

505 **Neutrophil-like cell culture and differentiation**

506 Cells from the human promyelocytic leukemia cell line (HL-60, ATCC) were cultured and
507 differentiated into neutrophil-like cells (dHL-60) as previously described (60). Briefly, HL-60 cells
508 were grown at 37C and 5% CO_2 to an approximate density of $1x10^6$ cells/mL and passaged every
509 two to three days by centrifugation and resuspension in Roswell Park Memorial Institute medium
510 supplemented with l-glutamine (RPMI-1640, Gibco Thermo Fisher Scientific), 10% v/v fetal bovine
511 serum (FBS, Omega Scientific), and 1% v/v penicillin-streptomycin (pen strep, Gibco Thermo
512 Fisher Scientific). HL-60 cells were differentiated by taking approximately 1.5 x 10^6 cells from a
513 passage and resuspending them in supplemented RPMI-1640 with 1.3% v/v dimethyl sulfoxide
514 (DMSO, Sigma) added. To ensure homogeneous distribution, the denser and more viscous
515 DMSO was thoroughly mixed with the RPMI-1640 before adding cells. Experiments were
516 conducted using dHL-60 cells cultured in the presence of DMSO between five and seven days.
517 For experimental use in control (Ctrl) treatment conditions, day 5 dHL-60 cells were resuspended
518 in supplemented M199 and incubated at 37C and 5% CO_2 for thirty-six to forty-eight hours, then
519 resuspended in fresh supplemented RPMI-1640 at the appropriate concentration for a given
520 secondary assay.

521 **Vascular endothelial cell culture**

522 Primary human vascular umbilical vein endothelial cells (HUVECs, Cell Applications) were grown
523 at 37C and 5% CO_2 in Medium 199 with l-glutamine, 2.2 g/L sodium bicarbonate, and Earle's salts
524 (M199, Gibco Thermo Fisher Scientific) supplemented with 10% v/v FBS, 10% v/v Endothelial
525 Cell Growth Medium (ECGM, Cell Applications), and 1% v/v pen strep until they formed a
526 confluent monolayer. HUVEC were passaged following standard protocols for adherent
527 mammalian cells: spent culture medium was aspirated, and cells were washed using Dulbecco's
528 phosphate buffered saline without calcium chloride or magnesium chloride (DPBS, Gibco Thermo
529 Fisher Scientific); wash solution was aspirated and replaced with the pre-warmed 0.25% trypsin-
530 EDTA (Gibco Thermo Fisher Scientific); the plate was incubated at 37C and 5% CO_2 until at least
531 90% detachment was observed on an inverted microscope, at which point a volume of pre-
532 warmed supplemented M199 equal to at least two times the volume of trypsin used was added to
533 the plate and circulated by repeated pipetting to dislodge tenuously adherent cells; cells were
534 collected via centrifugation, resuspended at the desired concentration in fresh supplemented

535 M199, seeded in a situationally appropriate vessel, and incubated at 37C and 5% CO_2 at least
536 twenty-four hours prior to next use. Experiments were performed using cells between 4 and 7
537 passages (P4 – P7).

538 **Primary neutrophil isolation from whole human blood**

539 Primary neutrophils (PMNs) were isolated from whole human blood samples taken from healthy
540 donors as previously described (61). Briefly, 7.5 mL of a red blood cell (RBC) sedimentation fluid
541 comprising 3% v/v Gelatin, 0.9% v/v NaCl, and 0.1% v/v Dextrose was added to the bottom of a
542 50 mL conical tube at a volume appropriate to achieve a 1:2 ratio by volume with the 15 mL whole
543 blood sample introduced on top. The conical was mixed by inversion three times, then incubated
544 at room temperature for fifteen minutes until the RBCs sedimented and the solution stratified,
545 leaving a layer of leukocyte-rich plasma at the top. That plasma was transferred into a 15 mL
546 conical tube containing 3 mL of Ficoll-Paque Plus (Sigma), taking great care to avoid mixing the
547 two solutions, and centrifuged at 4C and 1500 rpm for twenty minutes. After removing the
548 supernatant, the pellet of RBCs and PMNs was resuspended in an RBC lysis solution comprising
549 1 mL DPBS and 5 mL H_2O and mixed by inversion for forty-five seconds before adding 2 mL of
550 3% NaCl and centrifuging at 4C and 1500 rpm for five minutes. The supernatant was removed,
551 and PMNs were gently resuspended in 1 mL of DPBS containing 1 g/L glucose for use in
552 experiments.

553 **Leukocyte TEM assay (ETW)**

554 Transwell permeable supports were employed as the basis of an assay to replicate the impact of
555 applied mechanical forces and intercellular interactions during transendothelial migration (TEM)
556 on subsequent neutrophil physiology and migration mechanics (Figure 1A). Prior to loading,
557 Transwell inserts with 3.0 μm pore polycarbonate membrane (12mm insert, Corning) were
558 incubated with 200 μL of 50 ng/mL fibronectin (Millipore Sigma Aldrich) at 4C for at least twenty-
559 four hours. The inserts were then washed twice with DPBS and equilibrated per manufacturer
560 recommendation by incubating them at 37C and 5% CO_2 for twenty-four to forty-eight hours with
561 1 mL of fresh supplemented M199 in the lower chamber and 500 μL in the upper chamber.

562 Following equilibration, the medium in the lower chamber was replaced with 1 mL fresh
563 supplemented M199, and the medium in the upper chamber was replaced with 500 μL HUVEC
564 suspended at a concentration of 4.5×10^5 cells/mL in supplemented M199. Inserts were incubated
565 at 37C and 5% CO_2 for thirty minutes, then washed with supplemented M199 to remove HUVEC
566 that were not adhered to the polycarbonate membrane and incubated for twenty-four hours to

567 form a confluent monolayer. The medium was then aspirated from the upper chamber and
568 replaced with fresh M199 with 20 ng/mL tumor necrosis factor alpha (TNF-α) for at least eight
569 hours to activate the HUVEC monolayer.

570 Following TNF-α activation, the medium in the lower chamber was refreshed, day 5 dHL-60 cells
571 were resuspended in supplemented M199 and loaded into the upper chamber at a density of
572 approximately 8 x 10^6 cells, and the inserts were incubated at 37C and 5% CO_2. After thirty-six to
573 forty-eight hours, dHL-60 cells that had migrated through the HUVEC monolayer and the
574 polycarbonate membrane, termed ETW treated cells, were collected from the lower chamber and
575 resuspended in fresh, supplemented RPMI-1640 at an appropriate concentration for further pre-
576 treatment or use in experiments.

577 **Empty transwell-based leukocyte treatment assay (TW)**

578 To decouple the impact of physical interaction with and deformation required to pass through the
579 membrane in the TW support from biochemical and physical interactions with the HUVEC
580 monolayer on subsequent leukocyte interstitial migration, an empty transwell (TW) treatment
581 condition was employed (Figure 1C). Untreated inserts were equilibrated with supplemented
582 M199 as described above, then loaded with day 5 dHL-60 cells and incubated at 37C and 5%
583 CO_2. After thirty-six to forty-eight hours, cells that had migrated through the polycarbonate
584 membrane of the TW support were collected from the lower chamber of the insert and
585 resuspended in fresh supplemented RPMI-1640 at an appropriate concentration for further
586 treatment or use in experiments.

587 **HUVEC and dHL-60 co-culture assay (CC)**

588 To further decouple the influence of intercellular biochemical signaling and intimate physical
589 contact between HUVEC and dHL-60 cells during TEM from the large-scale cell body
590 deformations and external forces applied to dHL-60 cells as they traverse micron-scale junctional
591 gaps in the HUVEC monolayer, we introduced a co-culture (CC) treatment condition. HUVEC
592 were cultured to confluence in a 10 cm plate, then activated with TNF-α as previously described.
593 Then, the spent medium was aspirated and replaced by day 5 dHL-60 cells suspended in
594 supplemented M199 at approximately 1.6 x 10^7 cells/mL, and the plate was incubated at 37C and
595 5% CO2. After thirty-six to forty-eight hours, the medium, containing cells in suspension, was
596 circulated by repeated pipetting to dislodge any dHL-60 cells still loosely adhered to the HUVEC
597 monolayer, then collected and resuspended in supplemented RPMI-1640 at a concentration
598 appropriate for use in further experiments.

599 **Multi-color flow cytometry**

600 Samples were prepared for a four-color flow cytometry (FCS) panel following standard protocols
601 for antibody staining. For each experimental condition, four technical replicates were prepared for
602 the full FCS panel in addition to four technical replicates, each of fluorescence minus one control
603 (all fluorophores in the panel except one, to assist with gating), and single stain controls (to assist
604 with compensation). Unstained controls were resuspended in PBS and run without any additional
605 treatment. Unless otherwise specified, antibodies were purchased from Abcam. For ICAM-1 and
606 CD11b staining, cells were collected, resuspended in 10 μL of DPBS, mixed with the appropriate
607 primary antibody (goat ICAM-1 or rabbit CD11b) at a 1:1 (v/v) ratio, and incubated on ice for 30 –
608 60 min. CXCR1 and CXCR2 stains were purchased as pre-conjugated antibodies and did not
609 require this step. Samples were then resuspended in 10 μL of fresh DPBS, mixed with the
610 appropriate fluorophore-conjugated secondary antibody or pre-conjugated stain at a 1:1 (v/v)
611 ratio, and incubated covered on ice for 45 – 60 min. Samples were then washed once with DPBS
612 and resuspended in 300 μL of DPBS for experimental use. 30,000 events were collected for each
613 sample using a BD Accuri C6 Plus personal flow cytometer. Standard compensation, gating, and
614 subsequent analysis were performed using FlowJo.

615 **Total RNA extraction using TRIZOL reagent**

616 RNA isolation was performed following the TRIZOL RNA isolation protocol from the W.M. Keck
617 Foundation Biotechnology Microarray Resource Laboratory at Yale University. Briefly, the cells of
618 interest were resuspended in ice-cold DPBS, lysed via repetitive pipetting with TRIZOL reagent
619 (Ambion; 1mL reagent per 5-10 x 10^6 cells), and allowed to stand at room temperature for 5 min
620 to ensure complete disassociation. The suspension was centrifuged to remove any cell debris,
621 and then the supernatant was transferred to a new tube. Chloroform was added to the supernatant
622 at a ratio of 0.2 mL for every 1 mL of TRIZOL used, vortexed vigorously, and left to stand at room
623 temperature for two min before centrifuging to generate complete phase separation. The clear,
624 upper aqueous phase was transferred to a new tube.

625 RNA was precipitated from the solution by adding isopropyl alcohol to the aqueous phase at a
626 ratio of 0.5 mL for every 1 mL of TRIZOL used, incubated for 10 min at room temperature, and
627 centrifuged to pellet the RNA precipitate. After removing the supernatant, the RNA precipitate was
628 washed twice with a volume of 75% v/v ethanol greater than or equal to the volume of TRIZOL
629 used, air-dried for five to ten minutes, and redissolved into 100 μL of DEPC-treated water. RNA
630 concentration was measured using a Nanodrop 2000c (Thermo Scientific).

631 **First-strand cDNA synthesis**

632 First-strand cDNA was synthesized using M-MLV reverse transcriptase (RT; Invitrogen) following
633 the protocol included with the product information sheet. Briefly, for a standard 20 μL reaction
634 volume, 1 μL of oligo DT primers, a volume of resuspension containing 1 ng to 5 μg of total RNA
635 isolated as described in the previous section, 1 μL of 10 mM dNTP mix were added to a nuclease-
636 free microcentrifuge tube with sterile water such that the total volume was 12 μL. The tube was
637 heated to 65C for five min in a MyCycler thermal cycler (BioRad) and chilled on ice before adding
638 4 μL of 5x first-strand buffer, 2 μL of 0.1 M DTT, and 1 μL of RNaseOUT recombinant ribonuclease
639 inhibitor (40 units/μL). Contents were mixed and incubated in the thermal cycler at 37C for two
640 min before adding 1 μL of M-MLV RT and returning the tube to the thermal cycler, where the
641 mixture was held at 37 C for fifty min, immediately followed by fifteen min at 70 C. cDNA was
642 either used immediately as described below or stored at -80C until needed.

643 **Real time quantitative polymerase chain reaction (RT-qPCR)**

644 The newly synthesized first-strand cDNA was used as a template for amplification in RT-qPCR
645 following the protocol included in the product information sheet for iQ supermix (BioRad). Briefly,
646 assay master mix was prepared by mixing 7.5 μL of PowerTrack SYBR green master mix (2x,
647 Applied Biosystems) with 100 nM each of the forward and reverse primers (IDT, see Table 1 for
648 sequences) and a volume of sterile water such that, when the master mix was added to a volume
649 of RT product containing 100 ng of cDNA, each well of the qPCR plate contained a total reaction
650 volume of 15 μL. The total volume of master mix prepared was appropriately scaled to account
651 for technical triplicates of each gene of interest for each biological repeat and treatment condition.

652 Table 1: Forward and reverse sequences of oligos used for RT-qPCR.

Gene	Forward Sequence	Reverse Sequence
GAPDH	5' - ACA ACT TTG GTA TCG TGG AAG G - 3'	5' - GCC ATC ACG CAA CAG TTT C - 3'
ICAM-1	5’ – ATG CCC AGA CAT CTG TGT CC – 3’	5’ - GGG GTC TCT ATG CCC AAC AA – 3’
CXCR1	5' - CTG ACC CAG AAG CGT CAC TTG - 3'	5' - CCA GGA CCT CAT AGC AAA CTG - 3'

CXCR2	5' - CCT GTC TTA CTT TTC CGA AGG AC - 3'	5' - TTG CTG TATTGT TGC CCA TGT - 3'
FPR1	5' - TGG GAG GAC ATT GGC CTTTC -3'	5' - GGA TGC AGG ACG CAA ACA C - 3'
GRK2	5' - TCC AGC CAT ACA TCG AAG AGA - 3'	5' - CAA AAC CGT GTG AAC TTA TCG C -3'

Once each well was loaded, the plate was sealed with an optically transparent film, vortexed for 30 seconds to ensure thorough mixing of the reaction components, loaded into a CFX Connect Real-Time System (BioRad), and run following the manufacturer's thermal cycling conditions. Specifically, the reaction plate was held at 50 C for 2 minutes to activate uracil DNA glycosylase, then at 95 C for 2 minutes to activate DNA polymerase, before repeating the denaturing, annealing, and extending steps (95 C for 15 seconds, 58.1 C for 15 seconds, and 72 C for 1 minute, respectively) for 40 cycles.

The resulting data was analyzed in Microsoft Excel using the comparative C_T method (62). Briefly, expression levels for a gene of interest were normalized to a comparative baseline within each biological replicate by taking the difference between the C_T value for that gene and the C_T value of the housekeeping gene GAPDH (ΔC_T). ΔC_T values are expressed in relation to the control case for the purpose of comparison across treatment conditions by taking the difference between ΔC_T for a condition of interest and ΔC_T for the control case ($\Delta\Delta C_T$). Figures were generated using GraphPad Prism, showing log fold change compared to control, or $2^{-\Delta\Delta C_T}$, for ease of visualization. Statistically significant changes were determined using Kruskal-Wallis test for multiple comparisons, performed on ΔC_T values using GraphPad Prism. Between-run variation resulting from the use of multiple qPCR plates to amplify the same cDNA was removed by applying a previously reported mathematical transformation as part of the Excel analysis pipeline (63).

***In vitro* 3D directed migration assay**

In vitro assays of 3D directional migration were performed in a custom-built chemotaxis device (Figure 2A) as previously described (4). Briefly, 25 mm x 25 mm No. 1.5 coverslips (Corning) were placed on a 110 C hot plate and treated on one side with 300 μL of 0.1 M NaOH with 0.02% v/v Triton X. Once the NaOH solution evaporated, the coverslips were washed in distilled H_2O and allowed to dry. Then 50 μL of (3-aminopropyl) triethoxysilane (Sigma-Aldrich) was added to the

679 treated surface of the coverslip for 5 min. Coverslips were washed as described above, and the
680 treated surface was exposed to 100 μL of 0.5% v/v glutaraldehyde for 30 to 120 min. Coverslips
681 were allowed to air dry overnight in a vented, covered container or in a 65 C oven for 1 hour in
682 the same vented, covered container. Next, a 12-mm-diameter hole was punched in the center of
683 a 50 x 9-mm Falcon petri dish (BD Falcon) and attached a treated glass coverslip, treated side
684 facing up, to the bottom of the petri dish to create a glass bottom dish. A second treated coverslip
685 was then attached to the top side of the dish, treated side facing down and occluding
686 approximately three quarters of the hole to create a pocket of space in the center of the hole that
687 has silane-treated glass on both sides and a small loading port at the top. Both coverslips were
688 attached with vacuum grease (Beckman Vacuum Grease Silicone), and all edges in contact with
689 the petri dish were further sealed with clear quick dry nail polish (Sally Hansen Insta Dri). Before
690 gel fabrication, devices were equilibrated at 37C and 5% CO_2 for a minimum of thirty minutes to
691 help mitigate bubble formation during loading.

692 **Collagen gel fabrication and device loading**

693 Collagen gels were fabricated by neutralizing a solution of rat-tail type-I collagen monomers
694 dissolved in a 0.2 N acetic acid (Corning) with 1 N NaOH in proportions recommended by the
695 manufacturer's alternate gelation protocol to generate gels with a final collagen concentration of
696 1 mg/mL. A suspension of supplemented RPMI-1640 containing approximately 7.5 x 10^5 dHL-60
697 cells was used in place of the recommended water. All constituents for gel fabrication were kept,
698 mixed, and degassed on ice to prevent premature self-assembly, and the mixture was degassed
699 for 5 min prior to loading. Once prepared, 113 μL of the collagen gel solution was pipetted into the
700 pocket of each device. Devices were then incubated vertically at 37C and 5% CO_2 for thirty
701 minutes to allow the gel to self-assemble in the lower half of the pocket. The remaining volume of
702 the pocket was filled with 113 μL of supplemented RPMI-1640 with 50 nM fMLP and immediately
703 imaged.

704 **Image acquisition and cell tracking with bulk drift correction**

705 Bright-field images for population migration experiments were obtained using an enclosed Leica
706 DM16000 B microscope with a 5x air lens at 37C and 5% CO_2, with the built-in magnifier retracted
707 to produce images more amenable to automated cell tracking. Four planes, evenly spaced 200
708 μm apart to ensure the same cells were not captured in multiple planes, were imaged within each
709 collagen gel every Δt = 10 sec.

Automated cell tracking for standard time resolution experiments was performed using the Fiji plugin Trackmate (64, 65), discarding the first 50 frames of the time course for each experiment to eliminate migration artifacts caused by rapid gel drift. Cells were identified using a Laplacian of Gaussian (LoG) edge detection filter with median filtering enabled, and frame linking was performed using a linear assignment problem (LAP) tracker. Final cell tracks were filtered based on quality and duration, then exported to MATLAB for bulk drift correction and further analysis.

Drift velocity was calculated based on the bulk motion of non-motile cells within each experiment. Briefly, the first and second moments of inertia were calculated for each cell track and used as the basis for selecting the 15% of the experimental population with the lowest overall motility. Visual inspection confirmed that these cells were non-motile, and the one-minute smoothed median velocities of the non-motile population in each Cartesian direction were taken as the bulk drift velocity for the experiment. The drift velocity was then subtracted from each cell track within the experimental population to correct for bulk gel deformations during the experiment.

Summary migration statistics with respect to time

Cell centroids obtained from the tracking algorithm described above were used to calculate average instantaneous cell speed over Δt = 10 sec imaging intervals,

$$\langle v \rangle = \langle \langle \frac{\sqrt{(x_{t+1}-x_t)^2 + (y_{t+1}-y_t)^2}}{\Delta t} \rangle_t \rangle_{cells},$$

then converted to units of microns per minute. Average chemotactic index (CI) values were computed by taking the cosine of the angle θ between the chemotactic gradient vector and the displacement vector of each cell, $CI = \langle \cos\theta \rangle_{cells}$.

Analysis of trajectories in intrinsic coordinates

The shape of cell trajectories was analyzed in terms of distance traveled and angular orientation (intrinsic coordinates) as previously described (4), rather than in terms of time to eliminate the confounding influence of variations in migration speed between conditions. The distance travelled by a cell versus time was first computed as $s(t) = \sum_{\tau=0}^{\tau=t} \Delta s(\tau)$, where $\Delta s(t) = s(t + \Delta t) - s(t) = |\vec{x}(t + \Delta t) - \vec{x}(t)|$. This information was used to obtain $\vec{x}(s)$ via interpolation (interp1, MATLAB). The vector tangent to the trajectory was obtained as $\vec{t}(s) = d\vec{x}(s)/ds$. The mean squared displacements (MSDs) were computed as a function of distance lags, Δs, i.e., $r(\Delta s) = \langle |\vec{x}(s + \Delta s) - \vec{x}(s)| \rangle^2$, where the bracket denotes an ensemble average for all the cells in each experiment and along all values of s along each trajectory. Similarly, we computed the autocorrelation function for the vector tangent to the trajectory, $C_{tt} = \langle \vec{t}(s) \cdot \vec{t}(s + \Delta s) \rangle$. Changes

741 in orientation of $\vec{t}$ with respect to Δs were calculated as, $\Delta\theta(\Delta s) = \cos^{-1}\left[\vec{t}(s) \cdot \vec{t}(s + \Delta s)\right]$, in
742 addition to their PDF conditioned to Δs, $p(\theta|\, \Delta s)$.

743 **Estimation of migratory persistence length**

744 Based on the presence of two distinct decay regimes evident in semi-log plots of C_{tt}, the
745 migratory persistence length for each condition was estimated by fitting C_{tt} to a double
746 exponential decay model, expressed as $f(s) = \alpha\, e^{\frac{-s}{L_1}} + (1-\alpha)\, e^{\frac{-s}{L_2}}$ for each treatment condition
747 (lsqcurvefit, MATLAB). The double exponential fit requires that each condition be described in
748 terms of two characteristic lengths, $L_1$and L_2, defined so that $L_1 > L_2$. In all experiments, L_2
749 characterized a rapid autocorrelation decay, with average characteristic length <2 mm. Thus, the
750 migratory persistence length was taken to be $L_P = L_1$. Error bars were calculated via
751 bootstrapping. Briefly, 25% of the cells in a condition were randomly selected for removal from
752 the population and L_P was calculated for that subpopulation of cells. This process was repeated
753 twenty times. Mean and SEM were then calculated based on the twenty L_P values.

754 **Phagocytosis assay**

755 To measure changes in phagocytic behavior of dHL-60 cells before and after TEM, dHL-60 cells
756 were cultured and differentiated as described in (cell culture section), and ETW sorted cells were
757 prepared by performing the treatment assay described in (cell culture section). dHL-60 cells in
758 the condition of interest were resuspended with pHrodo Green Zymosan Bioparticles conjugate
759 for phagocytosis (Thermo Fisher Scientific) at the manufacturer's recommended concentration
760 and co-incubated at 37C and 5% CO_2 for 30 min. The sample was then resuspended in 300 μL of
761 DPBS. pHrodo particles are pH sensitive and will only emit fluorescence in highly acidic
762 intercellular environments such as endosomes and lysosomes. As such, we could quantify the
763 number of cells that had performed phagocytosis by employing single-color flow cytometry
764 following the measurement and analysis protocols outlined in (flow cytometry section).

765 **Inhibition of GRK2 expression in dHL-60 cells**

766 GRK2 inhibition experiments were performed using CMPD101 (Tocris Bioscience). For control
767 conditions, day 5 dHL-60 cells were resuspended in supplemented M199 and incubated at 37C
768 and 5% CO_2 for thirty-six to forty-eight hours. They were then resuspended in supplemented
769 RPMI-1640 with 30 μM CMPD101, incubated for 30 min at 37C and 5% CO_2, then resuspended
770 in fresh supplemented RPMI-1640 at an appropriate concentration for experimental use. For TW
771 sorted conditions, cells were collected from the lower chamber of the sorting assay, as described

above, resuspended in supplemented RPMI-1640 with 30 μM CMPD101, incubated for 30 min at 37C and 5% CO_2, then resuspended in fresh supplemented RPMI-1640 at an appropriate concentration for experimental use.

Time-dependent Bayesian sequential inference of heterogenous random walk

A 2D, first-order, auto-regressive process was used to model the persistent random walk of individual cells with time-varying motility parameters. The time series of the velocity vector of an individual cell, $\{\boldsymbol{v}_1, \dots, \boldsymbol{v}_{t-1}, \boldsymbol{v}_t, \boldsymbol{v}_{t+1}, \dots, \boldsymbol{v}_{N_t-2}\}$ was numerically obtained with 2nd order finite differences, where N_t is the number of images in the timelapse. Adapting the methodology of Metzner, Mark (26), the stochastic change in the velocity of a cell given the previous time step is described by the time-discrete stochastic process,

$$\boldsymbol{v}_t = q_t\, \boldsymbol{v}_{t-1} + a_t\, \boldsymbol{n}_t.$$

Here, $q_t \in [-1,1]$ corresponds to the local persistence of the random walk, $a_t \in [0, \infty)$ represents the local activity (stochastic amplitude) that sets the spatial scale of the random walk and $\boldsymbol{n}_t$ represents an uncorrelated, normally distributed noise with unit variance. The persistence q_t is a measure of the directional correlation between the successive time steps, not necessarily in the direction of the chemotactic gradient. $q_t = 1$ corresponds to a straight line and $q_t = 0$ to a non-persistence Brownian diffusion. Higher values of a_t correlate with increase in metrics such as cell speed, total displacement and track length. Together, the activity and persistence parameters determine the variance of displacement steps within a cell track according to $var(v) = a^2/(1-q^2)$ independently in each coordinate. Bayesian sequential inference (adapted from Metzner, Mark (26)) was performed in MATLAB to estimate the time-varying heterogeneous migration parameters of each individual cell.

Unsupervised identification of heterogenous sub-population from the random walk characteristics

Each individual cell was analyzed for changes in the migratory state during the duration of imaging to avoid averaging over different motility modes. A density-based spatial clustering (DBSCAN) algorithm (50) in MATLAB was employed to identify outliers and clusters in the inferred random walk parameters (q_t, a_t) within a single cell trajectory data. The parameter a_t for each cell was normalized to the range $[0,1]$ for subsequent analyses. The parameters $\epsilon = 0.1$ and $minPts = 10$ was used for the DBSCAN algorithm. This procedure is termed 'local clustering'. If more than one cluster was detected, they were treated as individual cells for further analysis. Each migrating

cell's trajectory was characterized by its average random walk parameters $(\bar{q}, \bar{a})$ of persistence and activity after local clustering.

To automatically identify sub-populations and shifts in the sub-populations across all experimental conditions (e.g. control, pharmacological treatments, etc.), cell-averaged random walk parameters $(\bar{q}, \bar{a})$ were pooled together. A Variational Bayesian Gaussian Mixture Model (VB-GMM) was used to cluster in the parameter space of $(\bar{q}, \bar{a})$. A Gaussian mixture model has the advantage of identifying elliptical clusters with anisotropic variances and the Bayesian formulation allows for automatically inferring the number of clusters from the data. This step, termed 'global clustering', was performed to autonomously identify heterogenous sub-populations based on the trajectory data alone.

The VB-GMM clustering algorithm fitted the datapoints in cell-averaged random motility parameter space with K Gaussian distributions delineating the densely populated regions (51), using code adapted from mixGaussVb.m in the MATLAB File Exchange, noting that we corrected an error in the posterior covariance matrix in the code. The GMM model assumes a mixture of K Gaussian clusters, each with a mean $\boldsymbol{\mu}_k$ and precision matrix $\boldsymbol{\Lambda}_k$, such that the distribution of the cell-averaged random walk parameters $\boldsymbol{x}_n = (\bar{q}, \bar{a})_n$ is

$$\mathrm{p}(\mathbf{x}) = \sum_{k=1}^{K} \pi_k \, N\left(\boldsymbol{x} \mid \boldsymbol{\mu}_k, \boldsymbol{\Lambda}_k^{-1}\right),$$

where π_k is the mixing coefficient, such that $\sum_{k=1}^{K} \pi_k = 1$ and $0 \leq \pi_k \leq 1$, controlling the proportion of each cluster. A symmetric Dirichlet distribution was chosen as the conjugate prior for π_k with the density,

$$p(\boldsymbol{\pi}) = \mathrm{Dir}(\boldsymbol{\pi} | \alpha_0) \propto \prod_{k=1}^{K} \pi_k^{\alpha_0 - 1}.$$

The concentration hyper-prior α_0 controls the sparsity of cluster numbers and the influence of data on the inference of the number of components K. α_0 values closer to 0 impart *a priori* belief that prefers fewer clusters that is influenced by data and as $\alpha_0 \to \infty$, the posterior of $\pi_k \to 1/K$ (no sparsity). For this manuscript, $\alpha_0 = 1$ was used which produces a flat Dirichlet distribution letting the parameter K be determined only from the data. Such a flat distribution is advantageous when working with many data points. For the parameters $\boldsymbol{\mu}_k$ and $\boldsymbol{\Lambda}_k$, a conjugate Gaussian-Wishart prior with zero mean was prescribed. The variational inference of the GMM mean $\boldsymbol{\mu}_k$ and precision matrix $\boldsymbol{\Lambda}_k$ as well as the number of clusters K was based on factorized approximation

to the posterior distribution through a latent variable representation. The specific details of the inference method are omitted here, and the reader is referred to Bishop *et al* (51).

834 **Figure Captions**

835 **Figure1. TEM process alters neutrophil phenotypes associating with the loss of directional**
836 **motility and better phagocytosis functions.** (A) Schematic of the Transwell-based treatment
837 assay employed to replicate the physiological effects of TEM on PMN physiology. VECs are
838 seeded on the polycarbonate membrane of a TW insert and grown to confluence and activated
839 with TNF-α before day 5 DMSO-differentiated HL-60 cells are loaded into the upper chamber.
840 PMNs that transmigrate through the VEC monolayer and TW membrane are collected from the
841 lower chamber for use in further experiments. (B) RT-qPCR results of gene expressions in dHL-
842 60 cells subjected to static control or ETW-crossing cells. Values are expressed in terms of log
843 fold change compared to control. Error bars were calculated for ΔC_T values. n=3, $*p < 0.05$,
844 $**p < 0.01$ Krystal Wallis test. (C) TW condition where dHL-60 cells transmigration through the
845 Transwell membrane with pore diameter of 3 μm. (D-E) FCS results of cell surface CXCR1 and
846 CXCR2 expressions in control, TW, ETW and CC-treated dHL-60 cells. Fluorescent expression
847 levels of CXCR1 and CXCR2 on TW, ETW and CC-conditioning cells are relative to levels of the
848 control dHL-60 cells. (F) Flow cytometry demonstrating the signal intensity of GFP in dHL-60 cells.
849 The gray color intensity is from dHL-60 cells without interacting with zymosan, showing the basal
850 level. (G) Quantitative analysis of GFP positive cells after 3 hours incubation with pHrodo
851 zymosan. (D-F) $p < 0.05$, $**p < 0.01$, $***p < 0.001$ (versus control group) using a one-way ANOVA
852 with Dunnett's post multiple comparison test. n = 3.

853 **Figure2. TEM induces heterogenous neutrophil motility in 3D accounting for overall**
854 **reduced area exploration and chemotactic migration. (A)** Schematic of pocket device for *in*
855 *vitro* 3D directed neutrophil migration assays. (B) Sample image of cells migrating in a pocket
856 device with Trackmate cell tracking results overlayed. Inset shows the time sequence for a
857 chemotaxing cell, with tracked trajectory overlayed in green. Scale bar, 1000 μm. (C) Probability
858 density maps of aggregated trajectory endpoints are shown for dHL-60 cells in each of the four
859 conditions with representative sample tracks overlayed. Sample track color saturation increases
860 with time. The dashed red reference circle superimposed on each inset figure represents
861 unbiased random motion. fMLP concentration increases linearly in the positive y direction. Black
862 arrows show the large angle turns. Scale bar, 20 μm. (D) Population average chemotactic index
863 (CI). (E) Population average mean cell speeds in four treatment conditions in the presence
864 of fMLP gradient. Error bars represent 95% confidence interval. All pairwise conditions showed
865 statistically significant differences besides those labeled n.s. (not significant) in (D-E). $****P <$
866 0.0001 according to the one-way ANOVA Tukey's test. (F) Mean squared displacements (MSDs)

867 versus distance separation along cell trajectories, $r^2(\Delta s)$. (G) Tangent vector autocorrelations
868 versus distance traveled, (Ctt ((Δs)), for *f*MLP condition, of four treatment conditions. The inset
869 represents the enlarged portion of the initial decay. (H) Migratory persistence length, L_P. Values
870 reflect the characteristic length of the slow decaying component of the double exponential fit, with
871 error bars calculated via bootstrapping (see Methods). ****$P < 0.0001$ according to the Brown-
872 Forsythe ANOVA test.

873 **Figure3. Mapping individual cell trajectories to time-dependent activity and persistence**
874 **parameters of a heterogeneous persistence random walk reveals distinct migratory**
875 **subpopulations.** (A-D) Probability density contour plots for motility modes, comprised of paired
876 activity and persistence values, for each of the four principal treatment conditions. Contours are
877 plotted for 5, 10, 20, 40, 60, 80, and 90% of total population density for each condition. (E)
878 Representative sample tracks taken from the high-(blue) and low-(grey) persistence clusters for
879 each of the four conditions. Color darkens along the course of each trajectory to indicate time
880 progression. fMLP gradient concentrations increases in direction of increasing y. (F) Relative
881 prevalence of each migratory subpopulation for each of the four conditions, expressed as
882 percentage of total population for each condition. Low-persistence cluster includes non-motile
883 cells.

884 **Figure 5. Quantitatively characterizing migration statistics reveals the dHL-60 low**
885 **persistence subpopulation replicates key features of low persistence PMN behavior.**
886 Descriptive statistics calculated for PMNs as compared to dHL-60 cell with treatment conditions
887 for cells assigned to high- and low-persistence subpopulations: (A-B) instantaneous mean cell
888 speed, (C-D) chemotactic index. (A-D) *$p < 0.05$, **$p < 0.01$, ***$p < 0.001$, ****$P < 0.0001$ according
889 to the one-way ANOVA Tukey's test. (E-F) Probability distribution maps of turning angles ($\Delta\theta$)
890 conditional to separation distance (Δs), $p(\Delta\theta|\Delta s)$ of the high-persistence cluster (E) and the low-
891 persistence cluster (F) in PMNs and dHL-60 cells of the four conditions.

892 **Figure 6. TEM-mediated leukocyte expression of GRK2 controls PMN's ability of directional**
893 **migration and phagocytosis.** (A) RT-qPCR results indicating changes in internal gene
894 expression potential for GRK2 in all four conditions. Values are expressed in terms of log fold
895 change compared to control. Error bars were calculated for ΔCT values. n = 3. *$p < 0.05$,
896 **$p < 0.01$, ***$p < 0.001$ to the one-way ANOVA Dunn's post t-test. (B) Probability density maps of
897 aggregated trajectory endpoints for ETW + CMPD treated dHL-60 cells with sample tracks
898 overlayed. Sample track color saturation increases with time. The dashed red reference circle
899 superimposed on each inset figure represents unbiased random motion. fMLP concentration

900 increases linearly in the positive y direction. Scale bar, 20 μm. (C) Population level instantaneous
901 mean cell speed, (D) chemotactic index, (E) MSDs and (F) autocorrelation function of the vector
902 tangent to the cell track versus distance traveled (Ctt ((Δs)), and (G) migratory persistence length
903 calculated for TW, ETW, and ETW + CMPD treated dHL-60 cells. (H) Flow cytometry
904 demonstrating the signal intensity of GFP in dHL-60 cells. Quantitative analysis of GFP positive
905 cells after 3 hours incubation with pHrodo zymosan. ***$p < 0.001$ (versus control group). n = 3
906 biological repeats. (C-D) *$p < 0.05$, ****$P < 0.0001$ according to the one-way ANOVA Tukey's test.
907 (G) ****$P < 0.0001$ according to the Brown-Forsythe ANOVA test. (H)**$P < 0.01$ according to
908 Student's *t*-test.

909 **Figure7. GRK2 controls the TEM-mediated prevalence of low motility subpopulation.** (A)
910 Probability density contour plot for paired activity/persistence motility modes of ETW + CMPD
911 treated cells, with contours plotted for 5, 10, 20, 40, 60, 80, and 90% of total population density.
912 30% and 90% contours of TW (grey circles) and ETW conditions (red triangles) are overlayed for
913 reference. (B) Relative prevalence of each migratory subpopulation for ETW, TW treated, TW +
914 CMPD, and Primary PMNs, expressed as percentage of total population for each condition. Low-
915 persistence cluster includes the "non-motile" cluster for the comparison. (C) Representative
916 sample tracks taken from the high-(blue) and low-(grey) persistence clusters for ETW + CMPD
917 treated cells. Color darkens along the course of each trajectory to indicate time progression. fMLP
918 gradient concentrations increases in direction of increasing y. (D-E) Descriptive statistics
919 calculated for cells assigned to high- and low-persistence subpopulations of TW, ETW, and ETW
920 + CMPD treated conditions: (D) instantaneous mean cell speed, and (E) chemotactic index. (D-
921 E) *$p < 0.05$, ****$p < 0.0001$ using a one-way ANOVA with Dunnett's test.

Reference

1. Ley K, Laudanna C, Cybulsky MI, Nourshargh S. Getting to the site of inflammation: the leukocyte adhesion cascade updated. Nat Rev Immunol. 2007;7(9):678-89.
2. Kolaczkowska E, Kubes P. Neutrophil recruitment and function in health and inflammation. Nat Rev Immunol. 2013;13(3):159-75.
3. Muller WA. Getting leukocytes to the site of inflammation. Vet Pathol. 2013;50(1):7-22.
4. Francois J, Kandasamy A, Yeh YT, Schwartz A, Ayala C, Meili R, et al. The interplay between matrix deformation and the coordination of turning events governs directed neutrophil migration in 3D matrices. Sci Adv. 2021;7(29).
5. Lam PY, Huttenlocher A. Interstitial leukocyte migration in vivo. Curr Opin Cell Biol. 2013;25(5):650-8.
6. Weninger W, Biro M, Jain R. Leukocyte migration in the interstitial space of non-lymphoid organs. Nat Rev Immunol. 2014;14(4):232-46.
7. Hind LE, Ingram PN, Beebe DJ, Huttenlocher A. Interaction with an endothelial lumen increases neutrophil lifetime and motility in response to P aeruginosa. Blood. 2018;132(17):1818-28.
8. Mukhopadhyay A, Tsukasaki Y, Chan WC, Le JP, Kwok ML, Zhou J, et al. trans-Endothelial neutrophil migration activates bactericidal function via Piezo1 mechanosensing. Immunity. 2024;57(1):52-67 e10.
9. Woodfin A, Voisin MB, Beyrau M, Colom B, Caille D, Diapouli FM, et al. The junctional adhesion molecule JAM-C regulates polarized transendothelial migration of neutrophils in vivo. Nat Immunol. 2011;12(8):761-9.
10. Nourshargh S, Hordijk PL, Sixt M. Breaching multiple barriers: leukocyte motility through venular walls and the interstitium. Nat Rev Mol Cell Biol. 2010;11(5):366-78.
11. Martinelli R, Zeiger AS, Whitfield M, Sciuto TE, Dvorak A, Van Vliet KJ, et al. Probing the biomechanical contribution of the endothelium to lymphocyte migration: diapedesis by the path of least resistance. J Cell Sci. 2014;127(Pt 17):3720-34.
12. Yeh YT, Serrano R, Francois J, Chiu JJ, Li YJ, Del Alamo JC, et al. Three-dimensional forces exerted by leukocytes and vascular endothelial cells dynamically facilitate diapedesis. Proc Natl Acad Sci U S A. 2018;115(1):133-8.
13. Liu Z, Sniadecki NJ, Chen CS. Mechanical Forces in Endothelial Cells during Firm Adhesion and Early Transmigration of Human Monocytes. Cell Mol Bioeng. 2010;3(1):50-9.
14. Rabodzey A, Alcaide P, Luscinskas FW, Ladoux B. Mechanical forces induced by the transendothelial migration of human neutrophils. Biophys J. 2008;95(3):1428-38.
15. Heemskerk N, Schimmel L, Oort C, van Rijssel J, Yin T, Ma B, et al. F-actin-rich contractile endothelial pores prevent vascular leakage during leukocyte diapedesis through local RhoA signalling. Nat Commun. 2016;7:10493.
16. Sorokin L. The impact of the extracellular matrix on inflammation. Nat Rev Immunol. 2010;10(10):712-23.
17. Theocharis AD, Skandalis SS, Gialeli C, Karamanos NK. Extracellular matrix structure. Adv Drug Deliv Rev. 2016;97:4-27.
18. Friedl P, Weigelin B. Interstitial leukocyte migration and immune function. Nat Immunol. 2008;9(9):960-9.

19. Lammermann T, Bader BL, Monkley SJ, Worbs T, Wedlich-Soldner R, Hirsch K, et al. Rapid leukocyte migration by integrin-independent flowing and squeezing. Nature. 2008;453(7191):51-5.
20. Czerwinski T, Bischof L, Böhringer D, Kara S, Strissel PL, Strick R, et al. Immune cells employ intermittent integrin-mediated traction forces for 3D migration. bioRxiv. 2024:2023.04.20.537658.
21. Dunn GA. Characterising a kinesis response: time averaged measures of cell speed and directional persistence. Agents Actions Suppl. 1983;12:14-33.
22. Tranquillo RT, Lauffenburger DA, Zigmond SH. A stochastic model for leukocyte random motility and chemotaxis based on receptor binding fluctuations. J Cell Biol. 1988;106(2):303-9.
23. Stokes CL, Lauffenburger DA. Analysis of the roles of microvessel endothelial cell random motility and chemotaxis in angiogenesis. J Theor Biol. 1991;152(3):377-403.
24. Parkhurst MR, Saltzman WM. Quantification of human neutrophil motility in three-dimensional collagen gels. Effect of collagen concentration. Biophys J. 1992;61(2):306-15.
25. Wu PH, Giri A, Sun SX, Wirtz D. Three-dimensional cell migration does not follow a random walk. Proc Natl Acad Sci U S A. 2014;111(11):3949-54.
26. Metzner C, Mark C, Steinwachs J, Lautscham L, Stadler F, Fabry B. Superstatistical analysis and modelling of heterogeneous random walks. Nat Commun. 2015;6:7516.
27. Ng LG, Ostuni R, Hidalgo A. Heterogeneity of neutrophils. Nat Rev Immunol. 2019;19(4):255-65.
28. Lecot P, Sarabi M, Pereira Abrantes M, Mussard J, Koenderman L, Caux C, et al. Neutrophil Heterogeneity in Cancer: From Biology to Therapies. Front Immunol. 2019;10:2155.
29. Silvestre-Roig C, Hidalgo A, Soehnlein O. Neutrophil heterogeneity: implications for homeostasis and pathogenesis. Blood. 2016;127(18):2173-81.
30. Beyrau M, Bodkin JV, Nourshargh S. Neutrophil heterogeneity in health and disease: a revitalized avenue in inflammation and immunity. Open Biol. 2012;2(11):120134.
31. Kienle K, Glaser KM, Eickhoff S, Mihlan M, Knopper K, Reategui E, et al. Neutrophils self-limit swarming to contain bacterial growth in vivo. Science. 2021;372(6548).
32. Mathias JR, Perrin BJ, Liu TX, Kanki J, Look AT, Huttenlocher A. Resolution of inflammation by retrograde chemotaxis of neutrophils in transgenic zebrafish. J Leukoc Biol. 2006;80(6):1281-8.
33. Lammermann T, Kastenmuller W. Concepts of GPCR-controlled navigation in the immune system. Immunol Rev. 2019;289(1):205-31.
34. Coombs C, Georgantzoglou A, Walker HA, Patt J, Merten N, Poplimont H, et al. Chemokine receptor trafficking coordinates neutrophil clustering and dispersal at wounds in zebrafish. Nat Commun. 2019;10(1):5166.
35. Penela P, Ribas C, Sanchez-Madrid F, Mayor F, Jr. G protein-coupled receptor kinase 2 (GRK2) as a multifunctional signaling hub. Cell Mol Life Sci. 2019;76(22):4423-46.
36. Evron T, Daigle TL, Caron MG. GRK2: multiple roles beyond G protein-coupled receptor desensitization. Trends Pharmacol Sci. 2012;33(3):154-64.

1008 37. Cant SH, Pitcher JA. G protein-coupled receptor kinase 2-mediated phosphorylation
1009 of ezrin is required for G protein-coupled receptor-dependent reorganization of the actin
1010 cytoskeleton. Mol Biol Cell. 2005;16(7):3088-99.
1011 38. Kahsai AW, Zhu S, Fenteany G. G protein-coupled receptor kinase 2 activates radixin,
1012 regulating membrane protrusion and motility in epithelial cells. Biochim Biophys Acta.
1013 2010;1803(2):300-10.
1014 39. Buckley CD, Ross EA, McGettrick HM, Osborne CE, Haworth O, Schmutz C, et al.
1015 Identification of a phenotypically and functionally distinct population of long-lived
1016 neutrophils in a model of reverse endothelial migration. J Leukoc Biol. 2006;79(2):303-11.
1017 40. Sun L, Ye RD. Role of G protein-coupled receptors in inflammation. Acta Pharmacol
1018 Sin. 2012;33(3):342-50.
1019 41. Babatunde KA, Wang X, Hopke A, Lannes N, Mantel PY, Irimia D. Chemotaxis and
1020 swarming in differentiated HL-60 neutrophil-like cells. Sci Rep. 2021;11(1):778.
1021 42. Li H, Qi S, Jin H, Qi Z, Zhang Z, Fu L, et al. Zigzag Generalized Levy Walk: the In Vivo
1022 Search Strategy of Immunocytes. Theranostics. 2015;5(11):1275-90.
1023 43. Crainiciuc G, Palomino-Segura M, Molina-Moreno M, Sicilia J, Aragones DG, Li JLY, et
1024 al. Behavioural immune landscapes of inflammation. Nature. 2022;601(7893):415-21.
1025 44. Ashton L. Sigler SBT, Logan Ellwood-Digel, Adithan Kandasamy, Mary J. Michaels-
1026 Foster, Dean Thumkeo, Shuh Narumiya, Juan Carlos Del Alamo, Jordan Jacobelli FMNL1 and
1027 mDia1 Promote Efficient T Cell Migration Through Complex Environments Via Distinct
1028 Mechanisms. Front Immunol. 2024;15.
1029 45. Jacobson EC, Perry JK, Long DS, Olins AL, Olins DE, Wright BE, et al. Migration through
1030 a small pore disrupts inactive chromatin organization in neutrophil-like cells. BMC Biol.
1031 2018;16(1):142.
1032 46. Ekpenyong AE, Toepfner N, Fiddler C, Herbig M, Li W, Cojoc G, et al. Mechanical
1033 deformation induces depolarization of neutrophils. Sci Adv. 2017;3(6):e1602536.
1034 47. Wang X, Jodoin E, Jorgensen J, Lee J, Markmann JJ, Cataltepe S, et al. Progressive
1035 mechanical confinement of chemotactic neutrophils induces arrest, oscillations, and
1036 retrotaxis. J Leukoc Biol. 2018;104(6):1253-61.
1037 48. Nourshargh S, Renshaw SA, Imhof BA. Reverse Migration of Neutrophils: Where,
1038 When, How, and Why? Trends Immunol. 2016;37(5):273-86.
1039 49. Claesson-Welsh L, Dejana E, McDonald DM. Permeability of the Endothelial Barrier:
1040 Identifying and Reconciling Controversies. Trends Mol Med. 2021;27(4):314-31.
1041 50. Martin Ester H-PK, Jörg Sander, and Xiaowei Xu. A density-based algorithm for
1042 discovering clusters in large spatial databases with noise. Proceedings of the Second
1043 International Conference on Knowledge Discovery and Data Mining. 1996:4.
1044 51. Bishop CM, Nasrabadi NM. Pattern recognition and machine learning: Springer; 2006.
1045 52. Hauert AB, Martinelli S, Marone C, Niggli V. Differentiated HL-60 cells are a valid
1046 model system for the analysis of human neutrophil migration and chemotaxis. Int J Biochem
1047 Cell Biol. 2002;34(7):838-54.
1048 53. Guo Y, Gao F, Wang Q, Wang K, Pan S, Pan Z, et al. Differentiation of HL-60 cells in
1049 serum-free hematopoietic cell media enhances the production of neutrophil extracellular
1050 traps. Exp Ther Med. 2021;21(4):353.
1051 54. Borregaard N. Neutrophils, from marrow to microbes. Immunity. 2010;33(5):657-70.

55. de Oliveira S, Rosowski EE, Huttenlocher A. Neutrophil migration in infection and wound repair: going forward in reverse. Nat Rev Immunol. 2016;16(6):378-91.
56. Kienle K, Lammermann T. Neutrophil swarming: an essential process of the neutrophil tissue response. Immunol Rev. 2016;273(1):76-93.
57. Zhang X, Guo R, Kambara H, Ma F, Luo HR. The role of CXCR2 in acute inflammatory responses and its antagonists as anti-inflammatory therapeutics. Curr Opin Hematol. 2019;26(1):28-33.
58. Wigerblad G, Cao Q, Brooks S, Naz F, Gadkari M, Jiang K, et al. Single-Cell Analysis Reveals the Range of Transcriptional States of Circulating Human Neutrophils. J Immunol. 2022;209(4):772-82.
59. Kapellos TS, Bassler K, Fujii W, Nalkurthi C, Schaar AC, Bonaguro L, et al. Systemic alterations in neutrophils and their precursors in early-stage chronic obstructive pulmonary disease. Cell Rep. 2023;42(6):112525.
60. Millius A, Weiner OD. Chemotaxis in neutrophil-like HL-60 cells. Methods Mol Biol. 2009;571:167-77.
61. Muñiz-Buenrostro A, Arce-Mendoza AY, Montes-Zapata EI, Calderón-Meléndez RC, Montelongo-RodrÍguez MJ. Simplified Neutrophil Isolation Protocol. International Journal of Immunology and Immunotherapy. 2020;7(1).
62. Livak KJ, Schmittgen TD. Analysis of relative gene expression data using real-time quantitative PCR and the 2(-Delta Delta C(T)) Method. Methods. 2001;25(4):402-8.
63. Ruijter JM, Ruiz Villalba A, Hellemans J, Untergasser A, van den Hoff MJ. Removal of between-run variation in a multi-plate qPCR experiment. Biomol Detect Quantif. 2015;5:10-4.
64. Ershov D, Phan MS, Pylvanainen JW, Rigaud SU, Le Blanc L, Charles-Orszag A, et al. TrackMate 7: integrating state-of-the-art segmentation algorithms into tracking pipelines. Nat Methods. 2022;19(7):829-32.
65. Tinevez JY, Perry N, Schindelin J, Hoopes GM, Reynolds GD, Laplantine E, et al. TrackMate: An open and extensible platform for single-particle tracking. Methods. 2017;115:80-90.

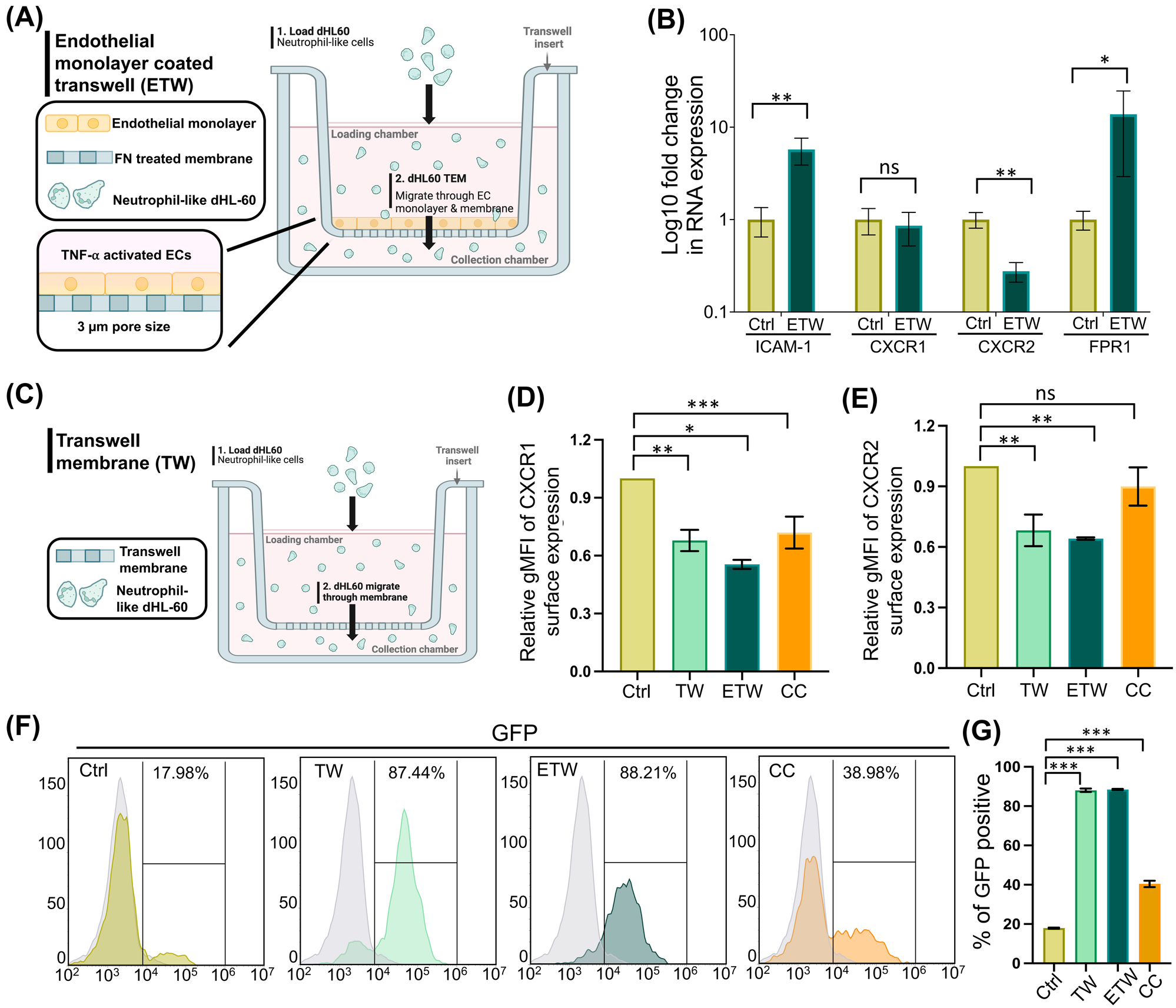
(A)
Endothelial monolayer coated transwell (ETW)
Endothelial monolayer
FN treated membrane
Neutrophil-like dHL-60
TNF-α activated ECs
3 µm pore size
1. Load dHL60
Neutrophil-like cells
Transwell insert
Loading chamber
2. dHL60 TEM
Migrate through EC monolayer & membrane
Collection chamber
(B)
Log10 fold change in RNA expression
100
10
1
0.1
**
ns
**
*
Ctrl
ETW
ICAM-1
CXCR1
CXCR2
FPR1
(C)
Transwell membrane (TW)
Transwell membrane
Neutrophil-like dHL-60
1. Load dHL60
Neutrophil-like cells
Transwell insert
Loading chamber
2. dHL60 migrate through membrane
Collection chamber
(D)
Relative gMFI of CXCR1 surface expression
1.2
0.9
0.6
0.3
0.0
***
*
**
Ctrl
TW
ETW
CC
(E)
Relative gMFI of CXCR2 surface expression
ns
**
**
(F)
GFP
Ctrl
17.98%
TW
87.44%
ETW
88.21%
CC
38.98%
150
100
50
0
10^2
10^3
10^4
10^5
10^6
10^7
(G)
% of GFP positive
100
80
60
40
20
0
***
***
***

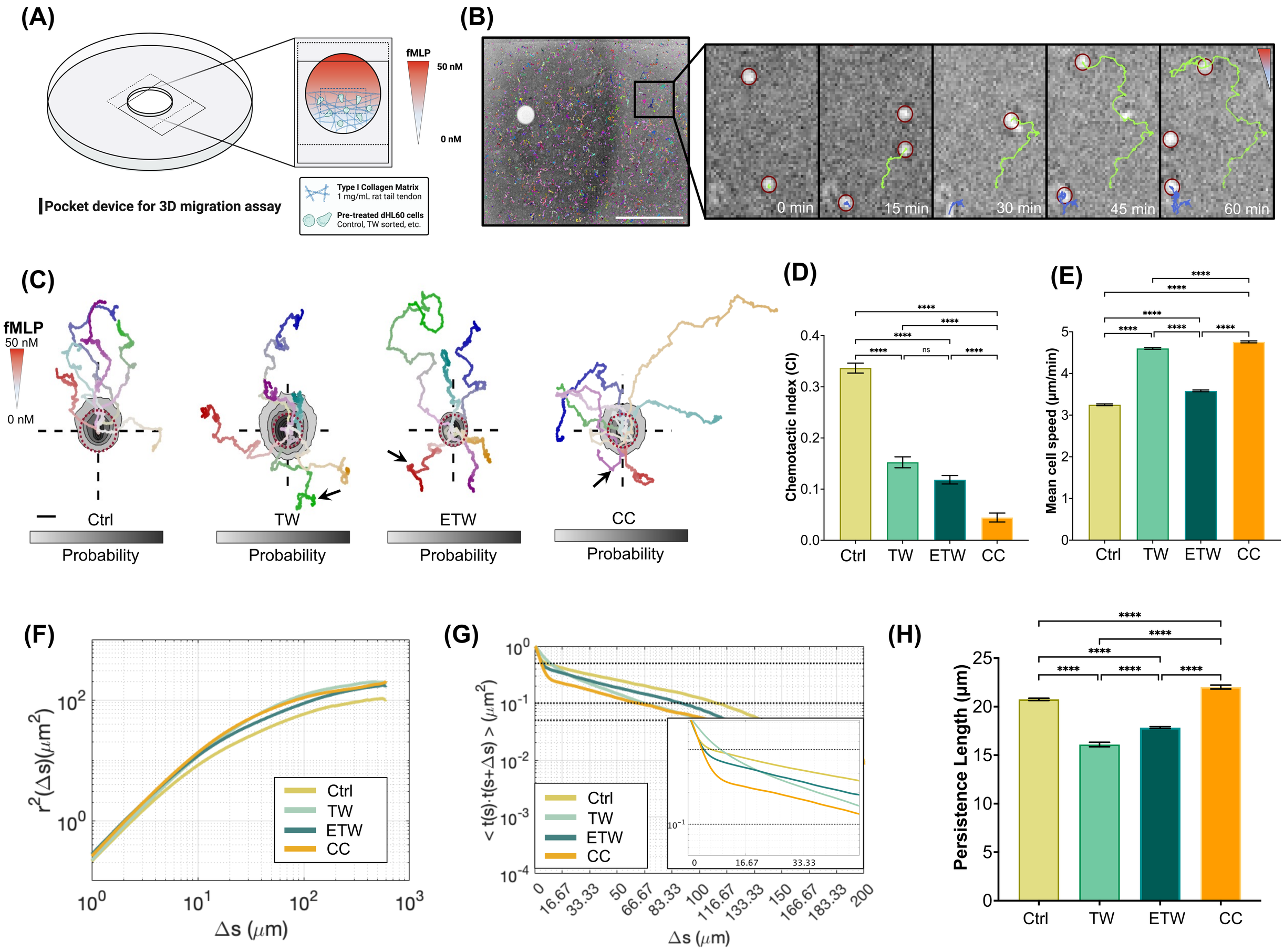
(A)
fMLP
50 nM
0 nM
Pocket device for 3D migration assay
Type I Collagen Matrix
1 mg/mL rat tail tendon
Pre-treated dHL60 cells
Control, TW sorted, etc.
(B)
0 min
15 min
30 min
45 min
60 min
(C)
fMLP
50 nM
0 nM
Ctrl
TW
ETW
CC
Probability
(D)
Chemotactic Index (CI)
Ctrl
TW
ETW
CC
(E)
Mean cell speed (μm/min)
(F)
r²(Δs)(μm²)
Δs (μm)
(G)
< t(s)·t(s+Δs) > (μm²)
Δs (μm)
(H)
Persistence Length (μm)

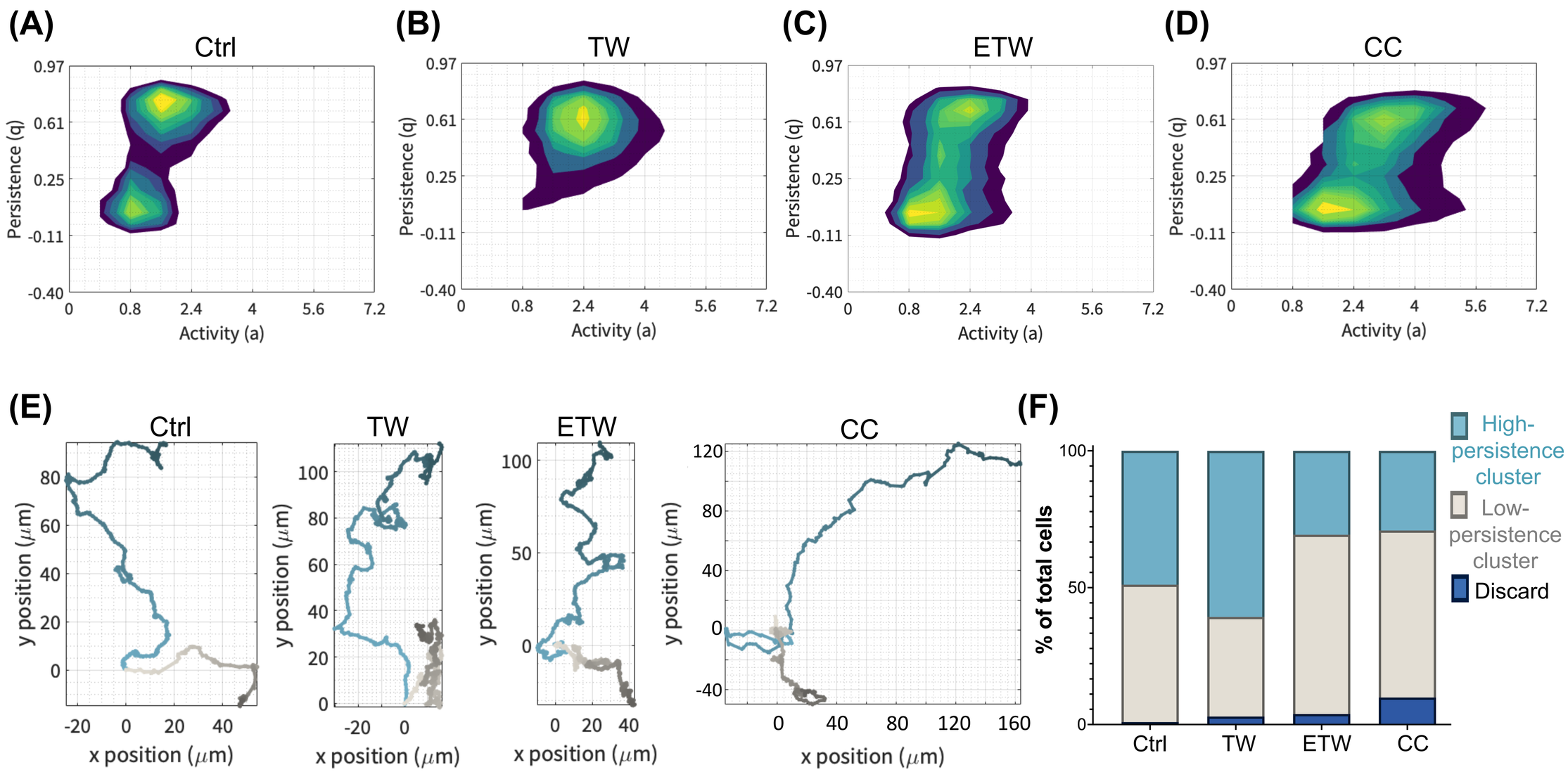
(A)
Ctrl
(B)
TW
(C)
ETW
(D)
CC
Persistence (q)
Activity (a)
0.97
0.61
0.25
-0.11
-0.40
0
0.8
2.4
4
5.6
7.2
(E)
Ctrl
TW
ETW
CC
y position (μm)
x position (μm)
(F)
% of total cells
High-persistence cluster
Low-persistence cluster
Discard
Ctrl
TW
ETW
CC

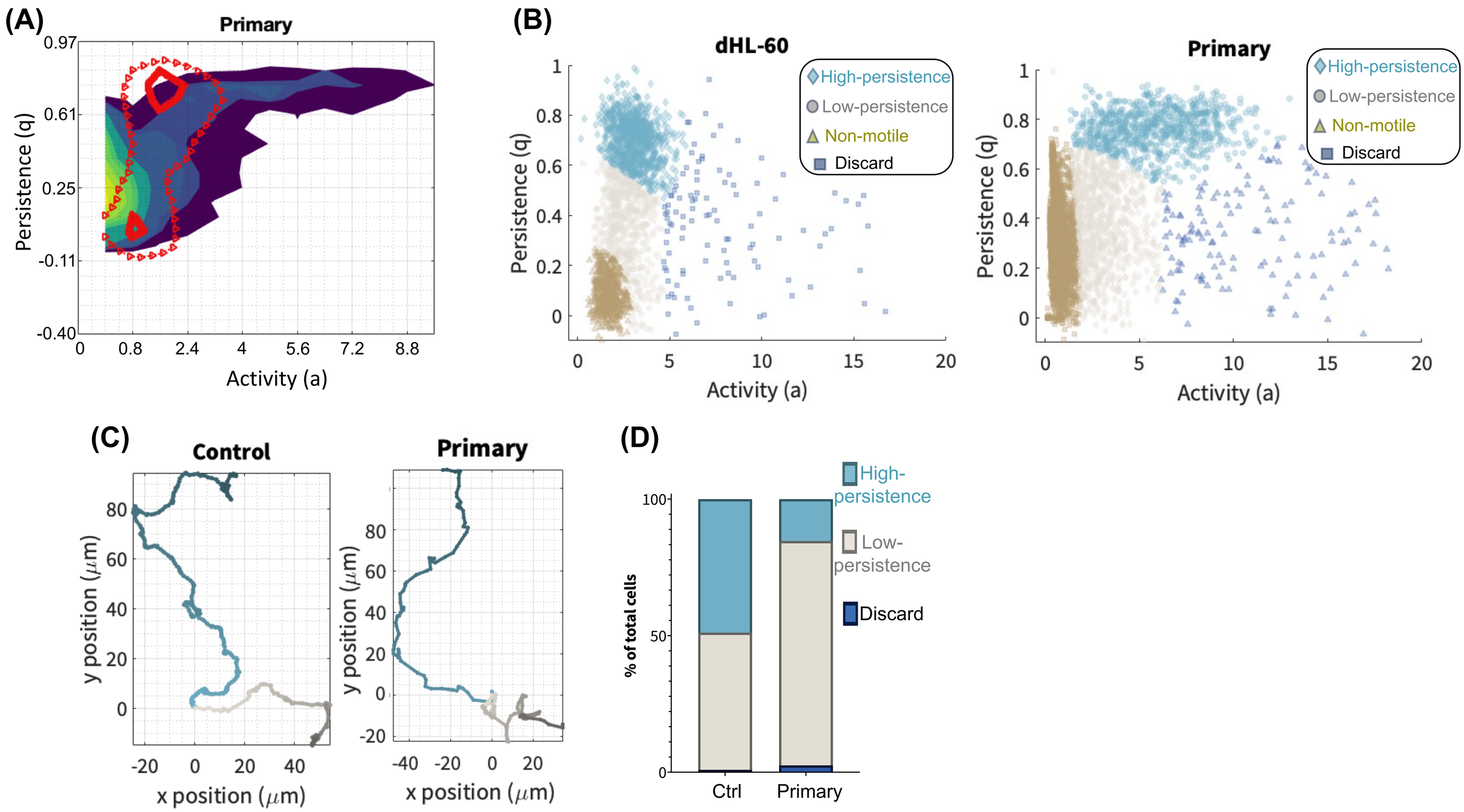
(A)
Primary
Persistence (q)
Activity (a)
(B)
dHL-60
Primary
High-persistence
Low-persistence
Non-motile
Discard
Persistence (q)
Activity (a)
(C)
Control
Primary
y position (μm)
x position (μm)
(D)
High-persistence
Low-persistence
Discard
% of total cells
Ctrl
Primary

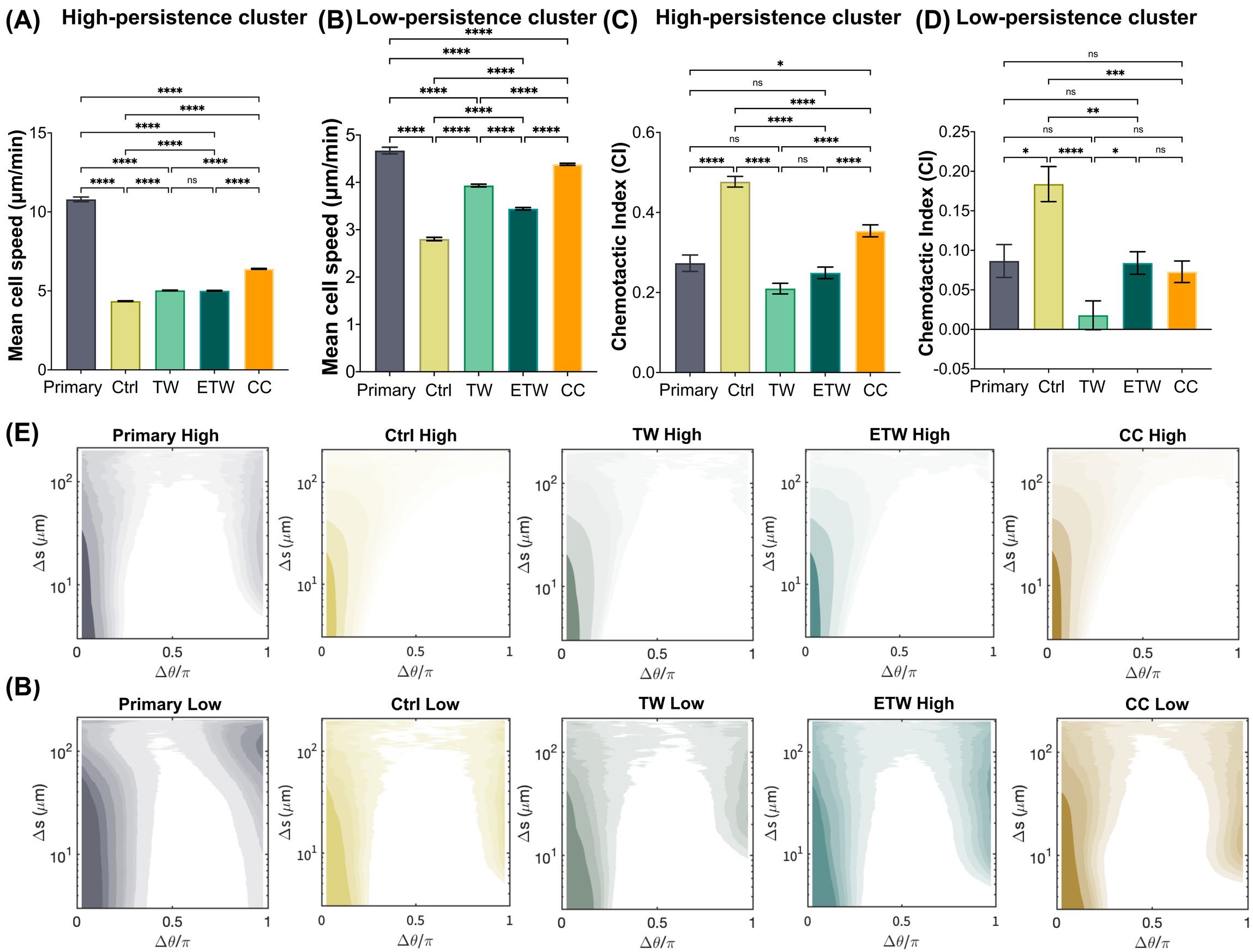
(A)
High-persistence cluster
Mean cell speed (μm/min)
Primary
Ctrl
TW
ETW
CC
(B)
Low-persistence cluster
Mean cell speed (μm/min)
(C)
High-persistence cluster
Chemotactic Index (CI)
(D)
Low-persistence cluster
Chemotactic Index (CI)
(E)
Primary High
Ctrl High
TW High
ETW High
CC High
(B)
Primary Low
Ctrl Low
TW Low
ETW High
CC Low
Δs (μm)
Δθ/π

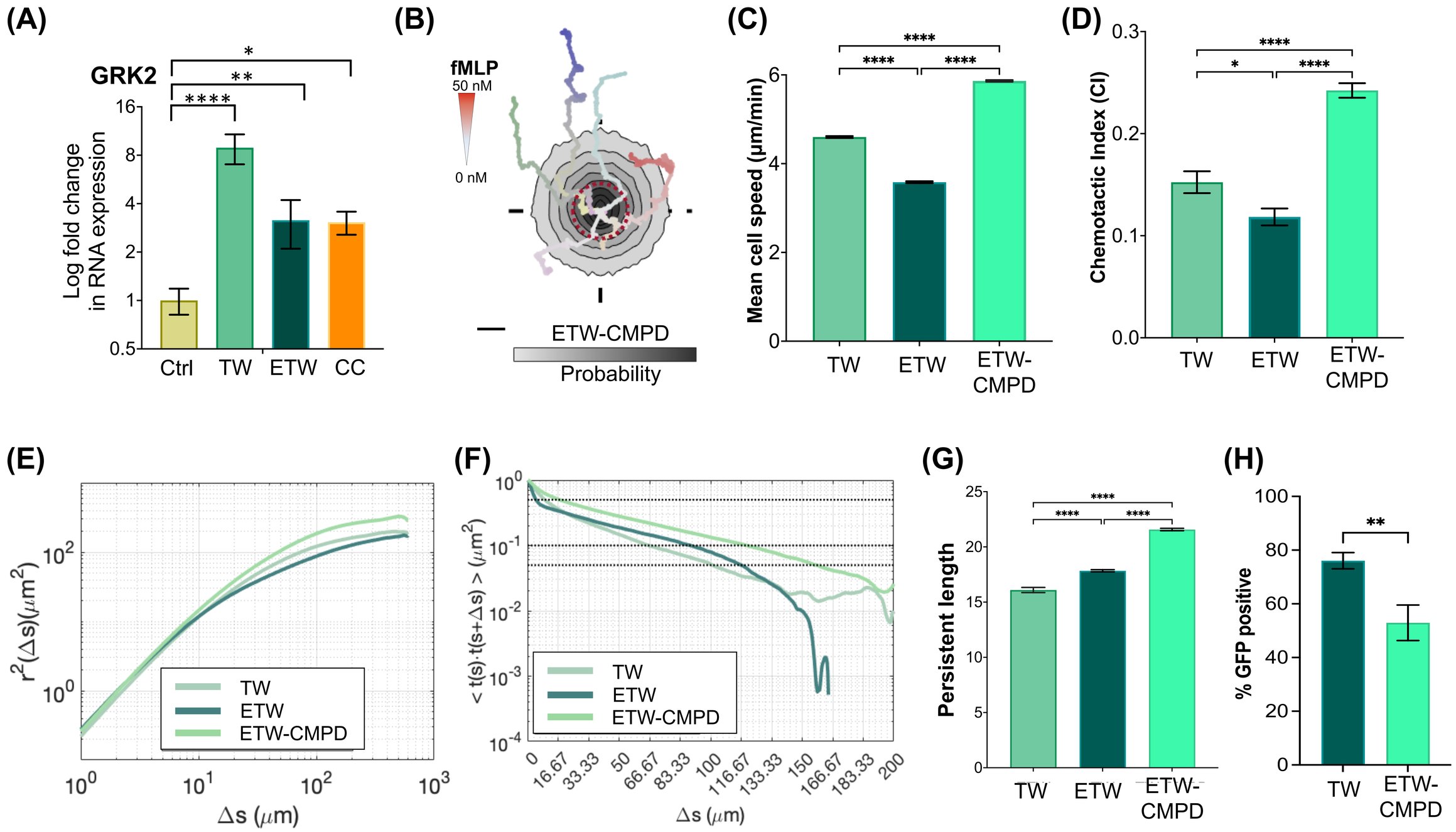
(A)
GRK2
Log fold change in RNA expression
Ctrl
TW
ETW
CC
(B)
fMLP
50 nM
0 nM
ETW-CMPD
Probability
(C)
Mean cell speed (μm/min)
TW
ETW
ETW-CMPD
(D)
Chemotactic Index (CI)
TW
ETW
ETW-CMPD
(E)
r²(Δs)(μm²)
Δs (μm)
TW
ETW
ETW-CMPD
(F)
< t(s)·t(s+Δs) > (μm²)
Δs (μm)
TW
ETW
ETW-CMPD
(G)
Persistent length
TW
ETW
ETW-CMPD
(H)
% GFP positive
TW
ETW-CMPD

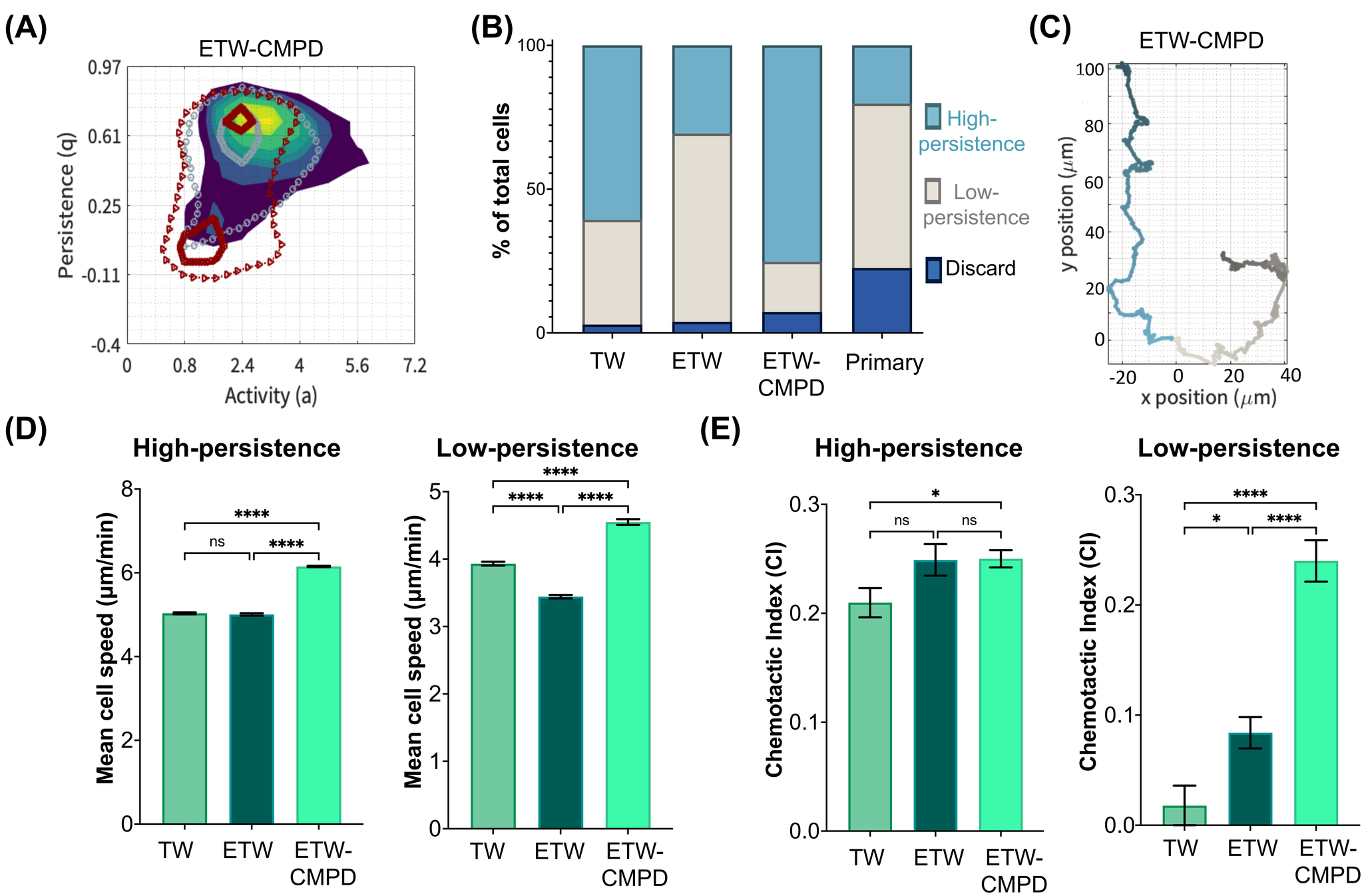
(A)
ETW-CMPD
Persistence (q)
Activity (a)
0.97
0.61
0.25
-0.11
-0.4
0
0.8
2.4
4
5.6
7.2
(B)
% of total cells
100
50
0
TW
ETW
ETW-CMPD
Primary
High-persistence
Low-persistence
Discard
(C)
ETW-CMPD
y position (μm)
x position (μm)
100
80
60
40
20
0
-20
0
20
40
(D)
High-persistence
Low-persistence
Mean cell speed (μm/min)
****
ns
****
TW
ETW
ETW-CMPD
(E)
High-persistence
Low-persistence
Chemotactic Index (CI)
*
ns
ns
****
*
****
0.3
0.2
0.1
0.0
TW
ETW
ETW-CMPD